

Targeting long non-coding RNA *NUDT6* enhances smooth muscle cell survival and limits vascular disease progression

Hanna Winter,^{1,2} Greg Winski,^{3,4} Albert Busch,^{1,5} Ekaterina Chernogubova,³ Francesca Fasolo,^{1,2} Zhiyuan Wu,^{1,2} Alexandra Bäcklund,³ Bohdan B. Khomtchouk,^{6,7,8} Derek J. Van Booven,⁹ Nadja Sachs,^{1,2} Hans-Henning Eckstein,^{1,2} Ilka Wittig,^{10,11} Reinier A. Boon,^{11,12,13,14} Hong Jin,^{3,15} and Lars Maegdefessel^{1,2,3}

¹Department for Vascular and Endovascular Surgery, Klinikum rechts der Isar, Technical University, Munich, Germany; ²German Center for Cardiovascular Research (DZHK), partner site Munich Heart Alliance, Berlin, Germany; ³Department of Medicine, Karolinska Institutet, Stockholm, Sweden; ⁴Function Perioperative Medicine and Intensive Care, Karolinska University Hospital, Stockholm, Sweden; ⁵Division of Vascular and Endovascular Surgery, Department of Visceral, Thoracic and Vascular Surgery, Medical Faculty, Carl Gustav Carus and University Hospital Carl Gustav Carus Dresden, Technische Universität Dresden, Dresden, Germany; ⁶Department of BioHealth Informatics, Indiana University, Indianapolis, IN, USA; ⁷Krannert Cardiovascular Research Center, Indiana University School of Medicine, Indianapolis, IN, USA; ⁸Center for Computational Biology & Bioinformatics, Indiana University School of Medicine, Indianapolis, IN, USA; ⁹John P. Hussman Institute for Human Genomics, Miller School of Medicine, University of Miami, Miami, FL, USA; ¹⁰Functional Proteomics, Institute of Cardiovascular Physiology, Goethe University, 60590 Frankfurt am Main, Germany; ¹¹German Center for Cardiovascular Research DZHK, Partner Site Frankfurt Rhine-Main, 60590 Frankfurt am Main, Germany; ¹²Institute of Cardiovascular Regeneration, Goethe University, 60590 Frankfurt am Main, Germany; ¹³Amsterdam UMC location Vrije Universiteit Amsterdam, Physiology, 1081 Amsterdam, the Netherlands; ¹⁴Amsterdam Cardiovascular Sciences, Microcirculation, 1105 Amsterdam, the Netherlands; ¹⁵Department of Molecular Medicine and Surgery, Karolinska Institutet, Stockholm, Sweden

Long non-coding RNAs (lncRNAs) orchestrate various biological processes and regulate the development of cardiovascular diseases. Their potential therapeutic benefit to tackle disease progression has recently been extensively explored. Our study investigates the role of lncRNA Nudix Hydrolase 6 (*NUDT6*) and its antisense target fibroblast growth factor 2 (*FGF2*) in two vascular pathologies: abdominal aortic aneurysms (AAA) and carotid artery disease. Using tissue samples from both diseases, we detected a substantial increase of *NUDT6*, whereas *FGF2* was downregulated. Targeting *Nudt6* *in vivo* with antisense oligonucleotides in three murine and one porcine animal model of carotid artery disease and AAA limited disease progression. Restoration of *FGF2* upon *Nudt6* knockdown improved vessel wall morphology and fibrous cap stability. Overexpression of *NUDT6* *in vitro* impaired smooth muscle cell (SMC) migration, while limiting their proliferation and augmenting apoptosis. By employing RNA pulldown followed by mass spectrometry as well as RNA immunoprecipitation, we identified Cysteine and Glycine Rich Protein 1 (CSRPI) as another direct *NUDT6* interaction partner, regulating cell motility and SMC differentiation. Overall, the present study identifies *NUDT6* as a well-conserved antisense transcript of *FGF2*. *NUDT6* silencing triggers SMC survival and migration and could serve as a novel RNA-based therapeutic strategy in vascular diseases.

INTRODUCTION

Atherosclerosis, the underlying pathology of most cardiovascular diseases, remains the most prominent cause of death worldwide.¹

Advanced atherosclerosis in carotid artery plaques is the most common reason for ischemic forms of large artery stroke while progressing abdominal aortic aneurysms (AAAs) are closely associated with the atherosclerotic burden and vascular inflammation within the infrarenal section of the aorta. Both diseases share similar molecular characteristics, including endothelial dysfunction,^{2,3} enhanced monocyte infiltration and macrophage activity,^{4,5} increased smooth muscle cell (SMC) apoptosis,^{6,7} as well as impaired extracellular matrix (ECM) remodeling.^{8,9} In AAAs, these mechanisms can culminate in an acute rupture with mortality rates above 80%.^{10,11} Vulnerable atherosclerotic lesions in the carotid artery can become unstable and rupture. This in consequence, leads to transient ischemic attacks, *amaurosis fugax*, and ultimately ischemic stroke, causing physical impairments and death.¹²

Apart from sharing similar pathophysiological features, both diseases also have similar risk factors, including dyslipidemia, arterial hypertension, family history/genetic association, advanced age, male sex, and smoking.¹³ Of further importance, about 60% of all AAA patients die from other cardiovascular diseases, such as stroke or myocardial infarction, again emphasizing the overlap in risk factor profiles and potentially

Received 27 November 2022; accepted 28 April 2023;
<https://doi.org/10.1016/j.ymthe.2023.04.020>.

Correspondence: Lars Maegdefessel, MD, PhD, Experimental Vascular Medicine Unit, Department for Vascular and Endovascular Surgery, Klinikum Rechts der Isar, Technical University Munich, Ismaninger Strasse 22, 81675 Munich, Germany.

E-mail: lars.maegdefessel@tum.de



shared underlying mechanistic drivers of both diseases.^{8,14} While several medications were discovered to slow down the atherosclerotic process in the carotid artery limiting the risk of plaque rupture, no treatment (apart from surgical intervention) is currently available for AAA patients to slow down expansion and reduce their risk of an acute rupture.¹⁵ Clinical handling of AAA patients is further hampered by the fact that currently, no tools (e.g., biomarkers) exist that allow foreseeing growth rates and rupture risk for any given individual.

SMC dynamics and fate in both pathologies play crucial roles during disease exacerbation. Under physiological conditions, vascular SMCs regulate the tone and contraction of arteries, thus maintaining the morphological integrity of the vasculature.¹⁶ When SMC survival is impaired, the vessel wall and plaque fibrous cap weaken, leading to lesion instability and aortic dilatation.^{6,9} When SMCs become hypo-migratory, fibrous cap thickness is decreased, and the aneurysm diameter expands.^{6,17} Furthermore, augmented matrix production and states of limited proliferation in SMCs accelerate the progression of both diseases.^{18,19}

Natural antisense transcripts (NATs) are a subclass of long non-coding RNAs representing the largest group of RNAs in mammalian genomes.²⁰ NATs are generally transcribed from the opposing strand to protein-coding genes. For most NATs, a repressive function on the expression of their partner sense transcript has been described in *cis*.²¹ This becomes interesting in diseases where the upregulation of classically considered “undruggable” targets, such as transcription or growth factors, is desirable.^{22,23} However, targeting the NAT that blocks transcription increases their expression levels, thus imposing potential benefits as future therapeutic approaches. Further, NATs were shown to exert their action faster than transcription factors due to their spatial proximity, which allows for immediate adaptation.^{24,25}

In this current study, we have investigated the lncRNA Nucleoside diphosphate-linked moiety X motif 6 (*NUDT6*), an NAT to the fibroblast growth factor 2 (*FGF2*). *NUDT6* and *FGF2* deregulation were discovered using laser capture microdissection of human stable and unstable fibrous caps as previously described.^{26,27} *NUDT6* overexpression limits survival, proliferation, and migration in arterial SMCs. Conversely, its silencing by using site-specific antisense oligonucleotides (GapmeRs), limits plaque rupture rates and experimental AAA growth in four preclinical disease models, thus providing an avenue for developing new therapeutic strategies to limit the burden of both vascular pathologies.

RESULTS

***NUDT6* and *FGF2* are deregulated in fibrous caps of advanced human atherosclerotic plaques**

To identify relevant mediators and effectors of fibrous cap stability, we performed laser capture microdissection of fibrous caps in atherosclerotic plaques (10 stable vs. 10 unstable plaques) from patients undergoing carotid endarterectomy (CEA) in our Department for Vascular and Endovascular Surgery at the Klinikum rechts der Isar of the Technical University Munich, Germany. Here, *NUDT6* was

enriched while *FGF2* expression was downregulated in unstable/ruptured compared with stable fibrous caps. Plaque stability was assessed based on fibrous cap thickness (>/< 200 μm) as previously described (Figures 1A–1C).^{17,26,28} *NUDT6* and *FGF2* form a prototypical mRNA-NAT sense/antisense (S/AS) pair with overlapping exons (Figure S1A) previously described in the cancer field.²⁹ *In situ* hybridization (ISH) on advanced atherosclerotic carotid plaques confirmed the increase in *NUDT6* signal predominantly associated with the fibrous cap while showing higher expression in ruptured lesions (Figure 1D). In the same lesions, deregulation of *FGF2* levels (high in stable, low in ruptured plaques) assessed by immunohistochemistry (IHC) could be detected (Figure 1E). SMC α -actin (αSMA), an indicator of SMC content and fibrous cap stability, was positively correlated with *FGF2* levels and appeared as expected higher in stable and lower in unstable/ruptured lesions (Figure S1B). Quantitative reverse-transcriptase PCR (qRT-PCR)-based expression analysis for *NUDT6* and *FGF2* on bulk lesions comparing stable vs. plaque phenotypes showed an increase of both *NUDT6* and *FGF2* (Figures 1F and 1G) in ruptured lesions. Thus, the deregulation of both transcripts seemed to appear exclusively in the culprit fibrous cap area and not in other regions of plaques, such as the necrotic core or the remaining media of the carotid arteries (Figure 1A).

***NUDT6* and *FGF2* deregulation is also present in human tissue specimens from patients with AAAs**

Based on the findings in the fibrous cap from stable and unstable plaques, we wanted to assess whether the deregulation of the *NUDT6*/*FGF2* axis is only present in carotid artery disease or potentially also of relevance in other vascular diseases, in which SMC survival appears of great importance. As this is the case in AAAs, we monitored the expression of both transcripts by qRT-PCR and ISH in human specimens from patients undergoing elective open aneurysm repair. *NUDT6* expression patterns reflected those observed in fibrous caps, with significantly higher AAA levels than non-dilated control aortas (Figures 1H and 1I). In line with the fibrous cap results, *FGF2* levels were substantially decreased in human AAA on both the protein and RNA levels (Figures 1J and 1K). Also, αSMA , being mainly expressed by contractile SMCs in AAA tissue, was less prominent in AAA vs. controls (Figure S1C).

***NUDT6* is increased, and *FGF2* downregulated in experimental murine models of inducible plaque rupture and AAA development**

As both *NUDT6* and *FGF2* are conserved in vertebrates,³⁰ we addressed whether similar disease-associated expression patterns could be observed in mouse models of vascular disease development. Atherosclerotic *ApoE*-deficient mice were utilized for the combined incomplete ligation/cuff injury model we established previously^{17,26,28} to induce plaque rupture in carotid arteries (Figure 2A), or the Angiotensin II (AngII) model³¹ to create suprarenal aortic aneurysms (Figure 2B). *Nudt6* transcript and *Fgf2* protein distribution within the vasculature were visualized via ISH and IHC, respectively. In line with our observations in human tissue, *Nudt6* was increased in both disease models (Figures 2C and 2D), whereas *Fgf2* protein was

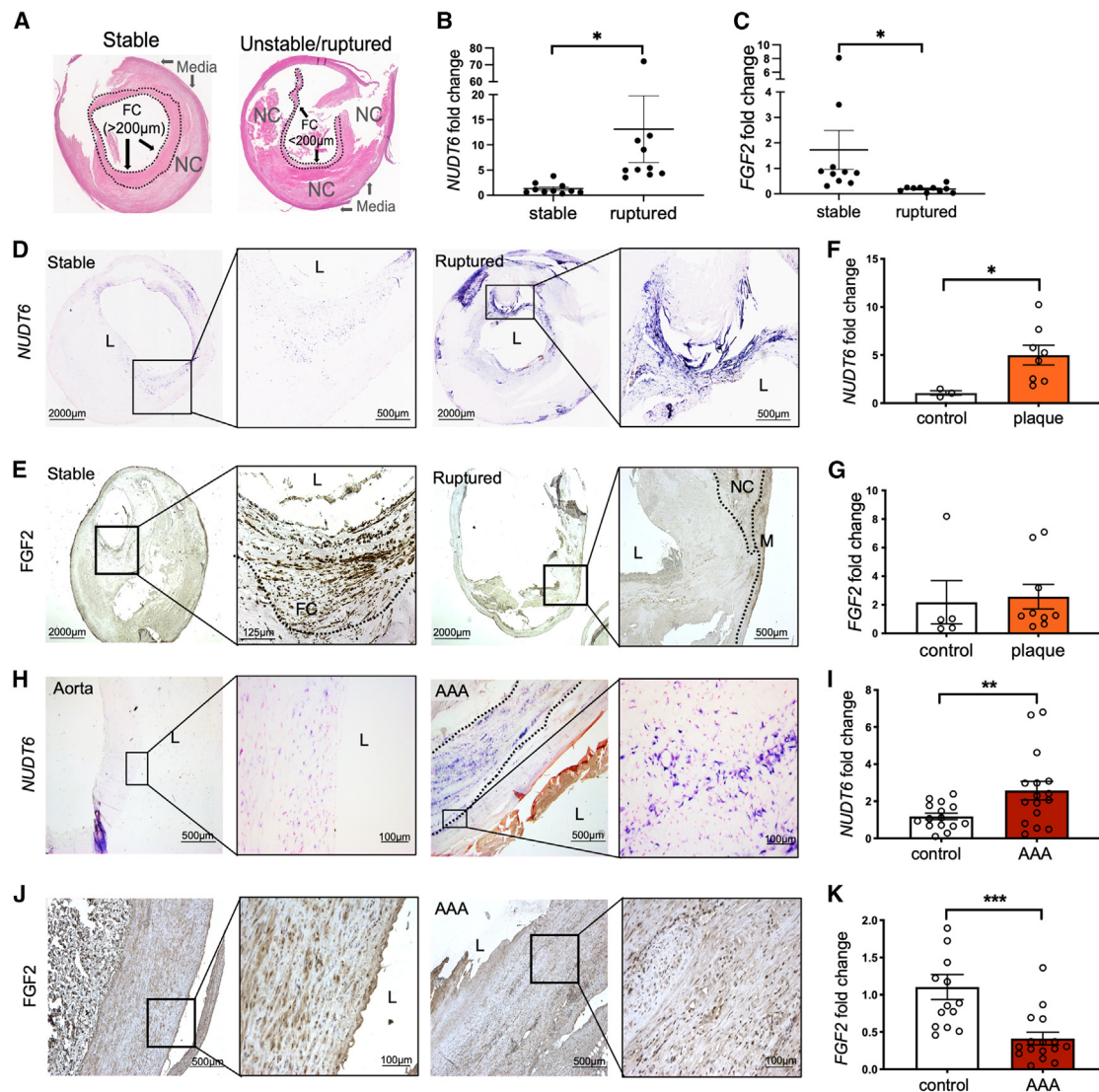


Figure 1. *NUDT6* expression is upregulated in human ruptured carotid plaques and human abdominal aortic aneurysm

(A) Hematoxylin and eosin stained stable and unstable or ruptured atherosclerotic plaques from the Munich Vascular Biobank. The dotted lines mark the fibrous cap (FC) shielding the necrotic core (NC) from the lumen. FC > 200 μm defines stable lesions, FC < 200 μm defines unstable lesions. (B and C) *NUDT6* (B) and *FGF2* (C) expression in micro-dissected carotid FCs of ruptured vs. stable lesions (n = 10 per group). (D) *In situ* hybridization (ISH) of stable and ruptured atherosclerotic carotid lesions (n = 5 per group) indicates a stronger signal in the fibrous caps of ruptured lesions. L = Lumen. (E) Immunohistochemical analysis of *FGF2* shows decreased expression in correlation with *NUDT6* in FC ruptured lesions compared with stable lesions (n = 3 per group). Dashed lines mark the FC. FC = fibrous cap; L = lumen; M = media; NC = necrotic core. (F and G) qRT-PCR analysis detecting *NUDT6* (F) and *FGF2* (G) in whole fresh-frozen carotid arteries of controls (n = 3–5) or advanced lesions (n = 8). (H) *In situ* hybridization of control aorta and abdominal aortic aneurysm (AAA) (n = 3 per group) indicates higher expression of *NUDT6* in the vessel's smooth muscle cell-rich media layer (dashed lines). L = lumen. (J) Immunohistochemical staining of *FGF2* shows decreased expression of both markers in AAA compared with aortic control (n = 3 per group). L = lumen. (I–K) qRT-PCR of whole fresh-frozen abdominal aortic aneurysm (n = 16) or control aorta (n = 13) detecting *NUDT6* (I) and *FGF2* (K). n = 13–16. Quantitative data are presented as mean +SEM. *p < 0.05; **p < 0.01; ***p < 0.0001. Significance was determined using one-tailed Student's t test (B), (C), (F), (G), and (I)–(K).

decreased in AngII-induced aneurysms and ruptured murine plaques (Figures 2E and 2F). To further mimic our efforts in analyzing advanced human carotid artery lesions, we performed qRT-PCR analysis from micro-dissected laser-captured murine fibrous caps. This confirmed *Nudt6* upregulation and *Fgf2* mRNA reduction in the cap (Figures 2G and 2H). Similar expression patterns were ob-

tained from qRT-PCR analysis of *Nudt6* and *Fgf2* in AngII-AAA tissue vs. saline-infused control specimens (Figures 2I and 2J). Interestingly, in a diet-induced model of early atherosclerotic lesion development, in which *ApoE*-deficient mice were either fed with regular chow or high-fat diet (HFD) for 12 weeks, no significant change in *Nudt6* or *Fgf2* expression could be detected (Figure S1D).

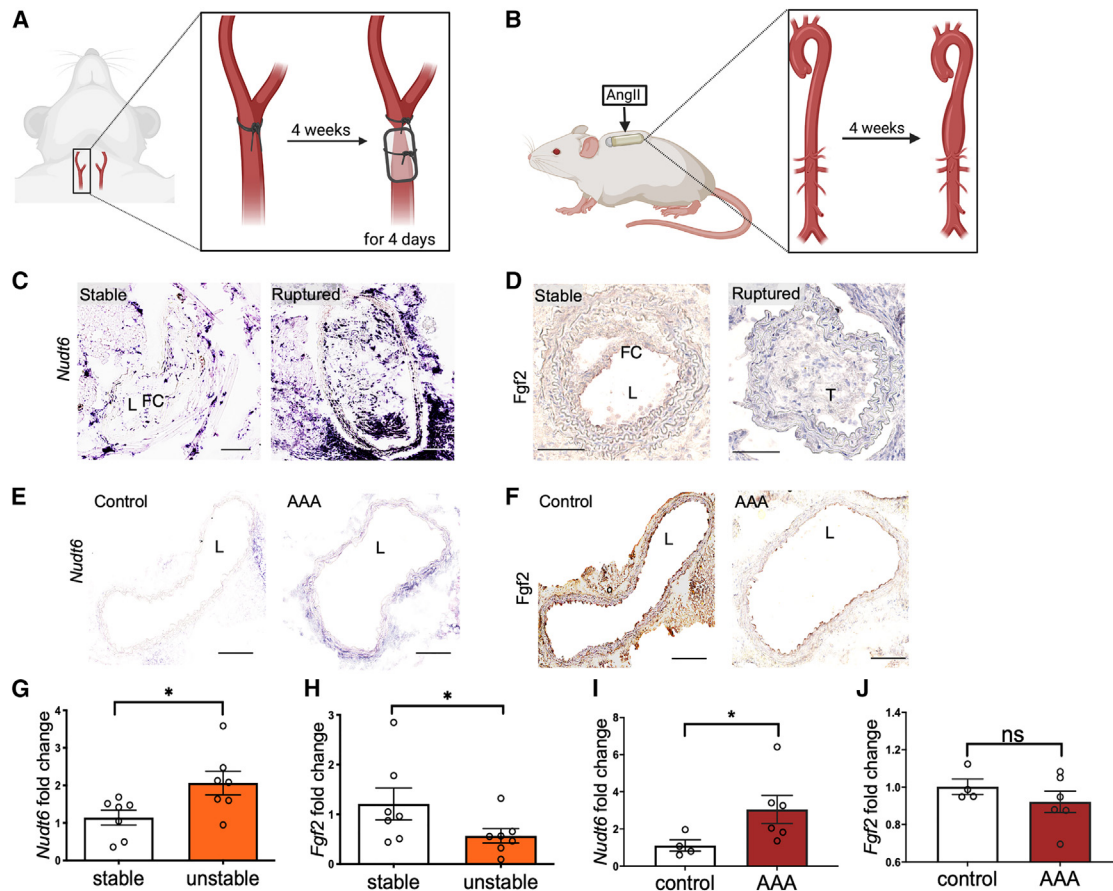


Figure 2. Increased *Nudt6* mRNA and decreased *Fgf2* mRNA and protein levels in two experimental animal models for vascular disease

(A) Scheme describing the inducible plaque rupture mouse model. A ligation is placed distally to the carotid bifurcation. After 4 weeks, a cone-shaped cuff is placed around the vessel, leading to disturbed blood flow. (B) Scheme of the Angiotensin II mouse model. After the implantation of an AngII-filled pump, an abdominal aortic aneurysm develops. (C and D) Stable vs. ruptured carotid plaques derived from ApoE^{-/-} mice undergoing the inducible plaque rupture (n = 7 per group) were stained for *Nudt6* (C, *in situ* hybridization) and *Fgf2* (D, immunohistochemistry), resembling the phenotype observed in human disease with increased *Nudt6* mRNA expression and decreased *Fgf2* protein levels in ruptured compared with stable lesions (n = 3 per group). (E and F) Saline-infused (control) vs. AngII-infused (AAA) ApoE^{-/-} aorta from the Angiotensin II mouse model (n = 6 per group) was stained for *Nudt6* (E) and *Fgf2* (F). (G–J) The observed phenotype was confirmed by qRT-PCR in murine stable vs. unstable/ruptured ApoE^{-/-} lesions (G) and (H) and murine ApoE^{-/-} saline-infused (control) vs. AngII-infused aortas (I) and (J) (n = 4–7 per group). Quantitative statistics are presented as mean + SEM. *p < 0.05 in one-tailed Student's t test. Scale bar, 100 μ m.

***Nudt6* inhibition *in vivo* reduces rupture risk and AAA growth**

To test the therapeutic feasibility of inhibiting *Nudt6* *in vivo*, locked nucleic acid (LNA) GapmeRs were delivered to the above-mentioned experimental mouse models. The designed GapmeR targeted *Nudt6* at exon 2, which does not overlap with *Fgf2* (see Figure S1A). Inhibiting *Nudt6* in the inducible plaque rupture model led to decreased rupture rates (Figure 3A). ISH and IHC further confirmed reduced *Nudt6* expression while rescuing *Fgf2* and α Sma expression in GapmeR-treated murine carotid arteries (Figures 3B and S1E). Next, local inhibition of *Nudt6* via ultrasound-targeted microbubble destruction (UTMD) was carried out in the aorta of AngII-treated mice with AAA. As shown in a previous study,²⁸ local delivery of anti-sense oligonucleotides (ASOs) can limit potential off-target effects while potentiating the inhibitory action of the site-specific GapmeRs applied in our experiments. Local penetration of the aortic

tissue was confirmed by sectioning and imaging of the abdominal aorta treated with a fluorescent FAM-labeled probe (Figure S1F). *Nudt6*-Antisense Oligonucleotide (ASO, GapmeR) treatment resulted in decreased abdominal aortic diameters upon weekly treatments until day 28 (Figure 3C). Furthermore, an overall improved vessel wall morphology (intactness of elastic laminae, increased SMC content) was accompanied by decreased *Nudt6*, as well as enhanced *Fgf2* and α Sma expression levels (Figures 3D, S1E–S1G).

To further confirm the observed findings of the AngII-AAA model, we performed a confirmatory study in a second mouse model of AAA development using porcine pancreatic elastase (PPE) in C57BL/6 mice. Utilization of this model allowed us to discriminate potential model-specific effects of AngII-induced aneurysms on *Nudt6* and *Fgf2* deregulation. A one-time systemic intraperitoneal

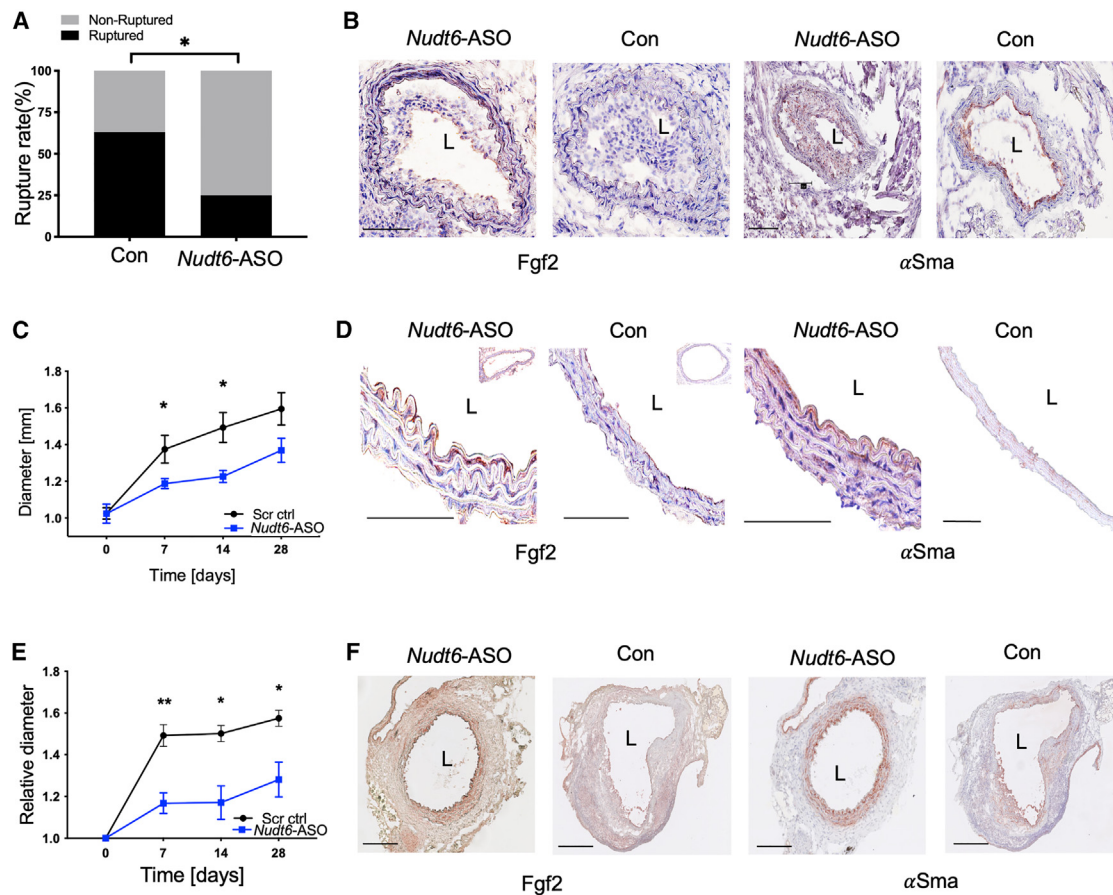


Figure 3. Modulating *Nudt6* in vivo leads to reduced rupture risk and reduced AAA growth

(A) *Nudt6*-ASO treatment ($n = 20$) of *ApoE*^{-/-} mice significantly reduced the rupture rate in the inducible plaque rupture model compared with scramble-control-treated animals ($n = 20$). (B) Fgf2 and α Sma immunohistochemistry display restored expression after *Nudt6*-ASO treatment ($n = 5$ per group). (C) In the AngII model, local *Nudt6*-ASO treatment ($n = 8$) of *ApoE*^{-/-} mice via ultrasound-targeted microbubble destruction (UTMD) led to significantly lower abdominal aortic diameter and reduced growth compared with scramble control treatment ($n = 13$). (D) Fgf2 and α Sma protein levels are restored in *Nudt6*-ASO-treated animals ($n = 3$ per group). (E) Systemic *Nudt6*-ASO treatment ($n = 4$) in the porcine pancreatic elastase (PPE) mouse model significantly reduced abdominal aortic diameter of *ApoE*^{-/-} mice and growth rate compared with control ($n = 5$). (F) Immunohistochemistry of Fgf2 and α Sma indicates higher expression in the *Nudt6*-ASO group compared with the control group ($n = 3$ per group). Quantitative data are shown as mean \pm SEM. * $p < 0.05$, ** $p < 0.01$. Significance was calculated using χ^2 test (A), and multiple t tests (C) and (D). Scale bar, 100 μ m.

injection of the *Nudt6*-ASO was performed on the same day the AAA was induced. Similar to our observation in AngII-treated mice, down-regulation of *Nudt6* (Figure S1E) resulted in decreased abdominal aortic diameters (Figure 3E). Notably, Fgf2 and α Sma content within the *intima media* was increased in the *Nudt6*-ASO group compared with scrambled GapmeR control mice with AAAs (Figure 3F). To conclude, *Nudt6* inhibition in three different mouse models led to alleviated and beneficial effects, such as reduced rupture rate of fibrous caps and AAAs, as well as smaller aortic diameters compared with respective control groups.

***NUDT6* inhibition derepresses FGF2, resulting in increased proliferation and reduced apoptosis in SMCs**

We next investigated *NUDT6*-mediated FGF2 regulation by using different stimuli *in vitro* relevant to vascular disease development and progression. Oxidized low-density lipoprotein (oxLDL) triggers

foam cell formation during atherogenesis in macrophages and SMCs.³² As we identified *NUDT6* being enriched in SMCs, we stimulated human carotid SMCs (hCtSMCs) with oxLDL and/or serum starvation. *NUDT6* RNA levels increased upon oxLDL stimulation, whereas *FGF2* was strongly reduced dose-dependently (Figure 4A). Similarly, human aortic SMCs (hAoSMCs) were treated with AngII, a factor known to trigger vascular inflammation and AAA formation.³³ AngII stimulation resulted in greatly increased *NUDT6* expression while reducing *FGF2* levels (Figure 4B). Furthermore, primary aortic SMCs isolated from three different AAA patients, as previously described,³⁴ showed a significant upregulation of *NUDT6* with a concomitant reduction of *FGF2* levels compared with commercially available hAoSMCs (Figures S2A and S2B). This could be reversed by knocking down *NUDT6* via small interfering RNAs (siRNAs) (Figures S2C and S2D). As *NUDT6* expression seemed to be triggered by disease, we subsequently tested the effects of *NUDT6* knockdown

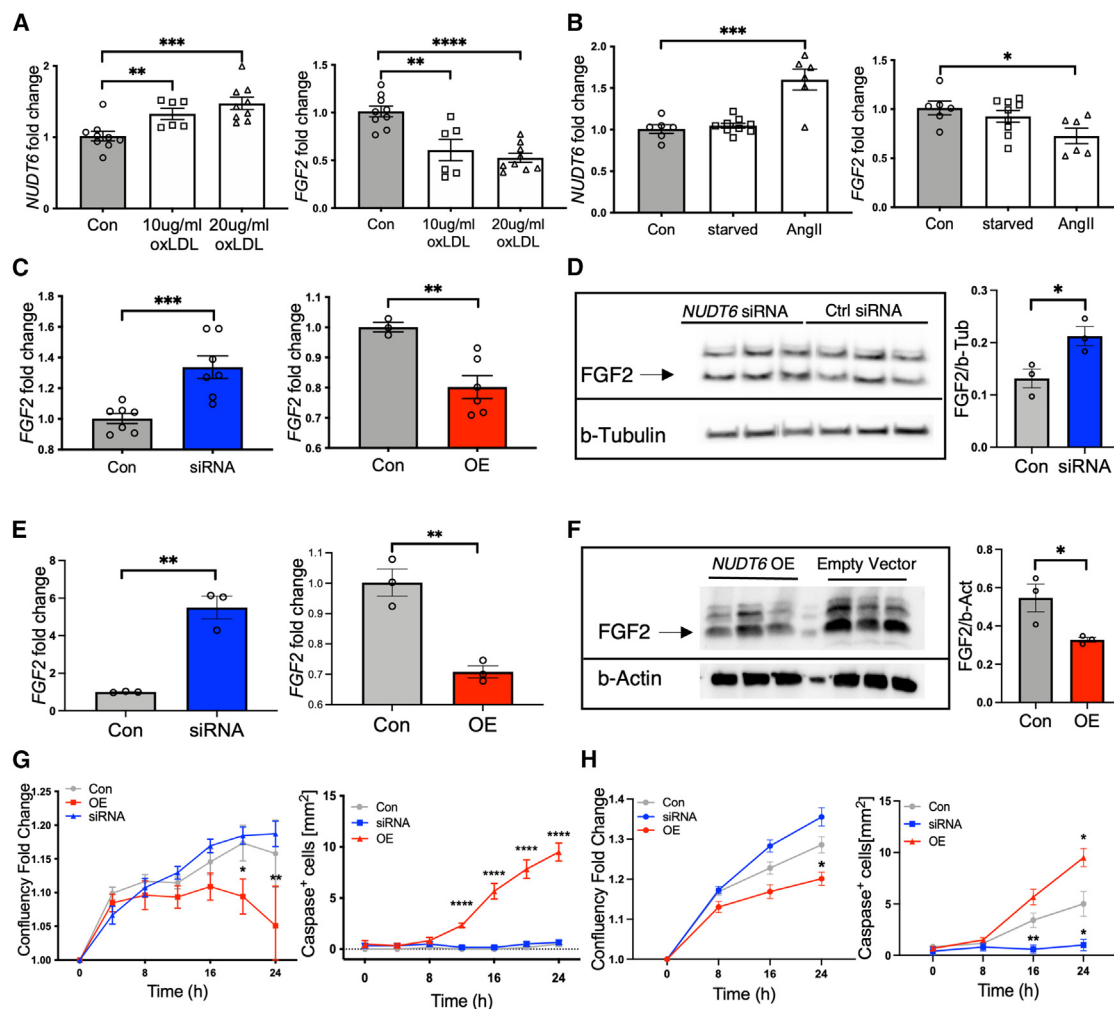


Figure 4. *NUDT6* represses *FGF2*, thereby inducing apoptosis and inhibiting proliferation

(A) Oxidized LDL treatment results in a dose-dependent increase of *NUDT6* expression, whereas *FGF2* decreases with increased dosage in human carotid smooth muscle cells (hCtSMCs) ($n = 6$ per group). (B) Angiotensin II treatment of human aortic smooth muscle cells (hAoSMCs) results in increased *NUDT6* and decreased *FGF2* expression ($n = 6-9$ per group). (C-E) By transfection of hCtSMCs (C) and hAoSMCs (E), siRNA-mediated knockdown of *NUDT6* results in increased *FGF2* expression, whereas vector-mediated overexpression of *NUDT6* limits *FGF2* mRNA levels. $n = 6$ per group. (D) *NUDT6* silencing restores *FGF2* protein, $n = 3$ per group. Scale bar, 100 μm . (F) *NUDT6* overexpression leads to less *FGF2* protein expression. (G and H) Dynamic live-cell imaging of both hCtSMCs (G) and hAoSMCs (H) show impaired proliferation capacity in *NUDT6* overexpressing cells while the apoptosis rate is significantly increased. *NUDT6*-siRNA-treated cells behave as scramble control-treated cells. $n \geq 6$. Quantitative results are presented as mean \pm SEM. * $p < 0.05$; ** $p < 0.01$; *** $p < 0.001$; **** $p < 0.0001$. Significance is determined using one-way ANOVA with Sidak (A) and (B), one-tailed Student's *t* test (C)-(F), or two-way ANOVA with Tukey (G) and (H).

(KD) and overexpression (OE) in hCtSMCs and hAoSMCs. siRNA-mediated silencing of *NUDT6* (Figure S2E) caused significant *FGF2* upregulation on both mRNA (Figures 4C and 4E) and protein levels (Figure 4D). Conversely, *NUDT6* OE (Figure S2E) substantially decreased *FGF2* mRNA (Figure 4C) and protein levels (Figure 4F).

By using a dynamic live-cell imaging system, we further explored the effects of *NUDT6* KD and OE, respectively, in terms of proliferation and apoptosis rates. Silencing of *NUDT6* did not impair proliferation or apoptosis in either hCtSMCs or hAoSMCs (Figures 4G and 4H). However, overexpression of *NUDT6* in both cell types limited prolif-

eration and increased apoptosis. Migration and motility of SMCs were also worsened in cells with *NUDT6* OE, but not in cells where *NUDT6* was silenced (Supplemental Figures 2F and 2G).

In addition to its regulatory function as an antisense transcript, a micropeptide coding function for *NUDT6* was recently described.^{35,36} To rule out any functional effect of the *NUDT6* micropeptide on SMCs, we stimulated hCtSMCs with the *NUDT6* peptide (Figure S2H). Importantly, we were not able to detect any functional role for this micropeptide in SMCs, supporting the fact that *NUDT6* RNA seems solely relevant for vascular disease development and progression.

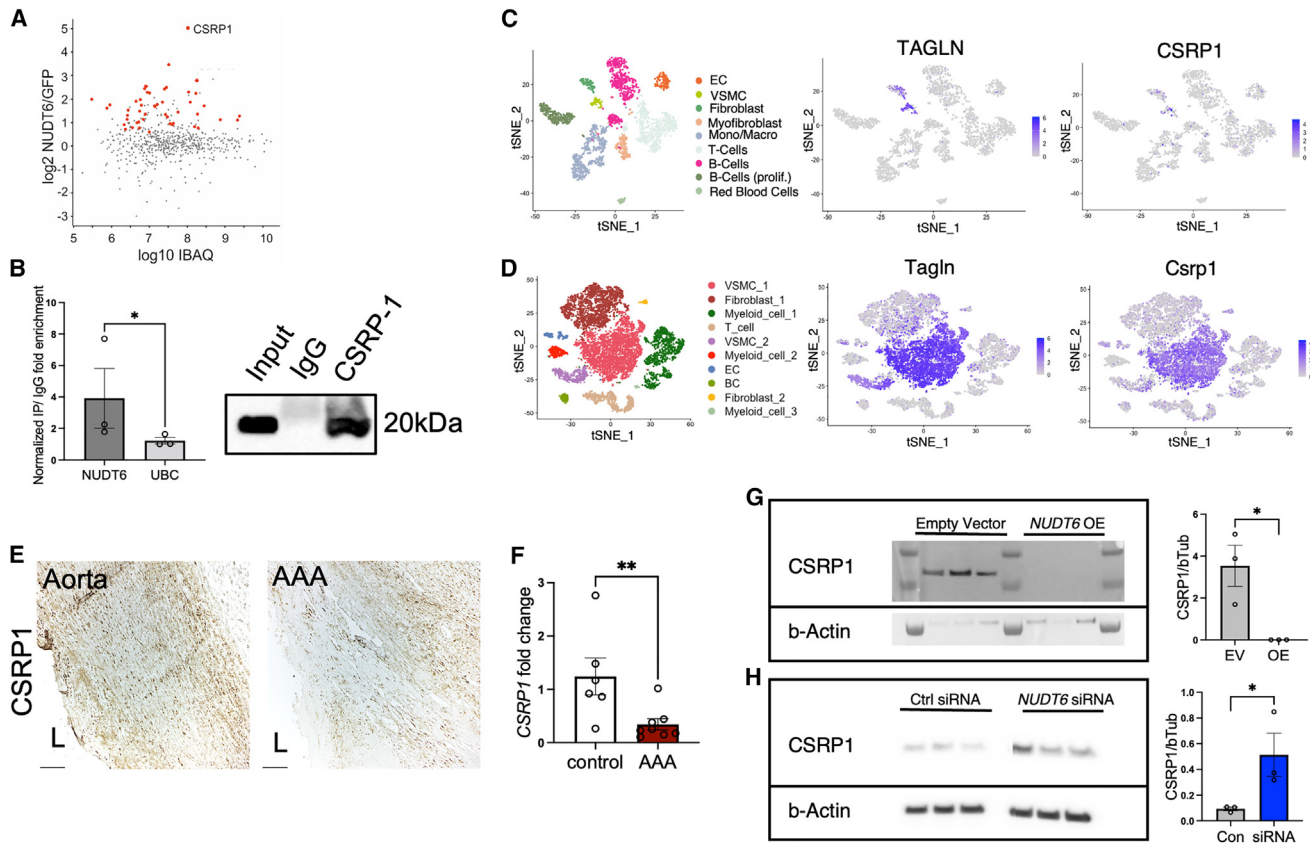


Figure 5. Identification and validation of NUDT6 interaction partner CSR1

(A) Identified proteins in biotinylated NUDT6 vs. biotinylated GFP pull-down in hAoSMCs ($n = 6$ per condition), red dots represent significantly enriched proteins (Student's t test) to NUDT6. (B) Confirmed binding of NUDT6 to CSR1 protein in hAoSMCs. NUDT6 and UBC (unrelated target) enrichment in CSR1 IP fraction was quantified using RT-qPCR and CSR1 availability was verified via western blot. T-distributed stochastic neighbor embedding (t-SNE) plots of single-cell RNA sequencing data from human (C) and (D) murine AAA (PPE-induced) with featured expression plots of Transgelin (TAGLN) and CSR1. (E) Immunohistochemical staining of CSR1 in human control aorta and AAA. (L indicates lumen). (F) qRT-PCR of whole fresh-frozen abdominal aortic control ($n = 6$) and AAA ($n = 8$) of CSR1 mRNA. (G) CSR1 protein levels after NUDT6 overexpression. (H) CSR1 protein levels after NUDT6 siRNA-mediated knockdown ($n = 3$ per group). Quantitative data are shown as mean \pm SEM. * $p < 0.05$; ** $p < 0.01$. Significance was calculated using one-tailed Student's t test. EC = endothelial cells, VSMCs = vascular smooth muscle cells; Mono/Macro = monocytes/macrophages; B-Cells (prolif.) = proliferating B cells. Scale bar, 150 μ m.

To determine where *NUDT6* and *FGF2* are located in the cell, nuclear-cytoplasmic fractionation was performed. This revealed localization of both *NUDT6* and *FGF2* primarily in the nucleus and to a lesser extent in the cytoplasm of hAoSMCs (Figure S3I). In hCtSMCs, *NUDT6* was found to be equally distributed between cytoplasm and nucleus (Figure S2J). Globally, these results suggest a worsened outcome in terms of aortic and carotid SMC survival and migration upon *NUDT6* upregulation, as induced by pathogenic stimuli, such as oxLDL and AngII, or by *NUDT6* overexpression. The ability of hCtSMCs to shield the necrotic core is impaired, while hAoSMCs fail to maintain the aortic wall integrity, leading to rapid expansion and acute rupture.

***NUDT6* interacts with CSR1 and thereby affects SMC contractility and migration**

To further explore the distinct molecular mechanism underlying *NUDT6* regulation, we aimed to identify a potential mediating function

through direct interaction with other proteins. We thus performed a *NUDT6*-RNA pull-down experiment followed by liquid chromatography-tandem mass spectrometry (LC-MS/MS). Using hAoSMC lysate and *in vitro* transcribed biotinylated *NUDT6* or control, 50 targets were identified as significantly enriched in the *NUDT6* pull-down fraction (Figure 5A). Cysteine and Glycine Rich Protein 1 (CSR1, 32.6-fold increase, Table S1) appeared most enriched and was thus chosen for further in-depth analysis based on its previously reported relevance to SMC function (Figure S3A).^{37–39} In general, many interaction partners seemed to be involved in SMC-mediated vascular pathologies (Figures S3B and S3C). The direct *NUDT6*-CSR1 interaction was further confirmed using RNA immunoprecipitation (RIP), where *NUDT6* could be detected in the eluted CSR1 fraction (Figure 5B).

Next, we performed single-cell RNA sequencing (scRNA-seq) on human AAA tissues, as well as murine and porcine PPE-induced AAAs

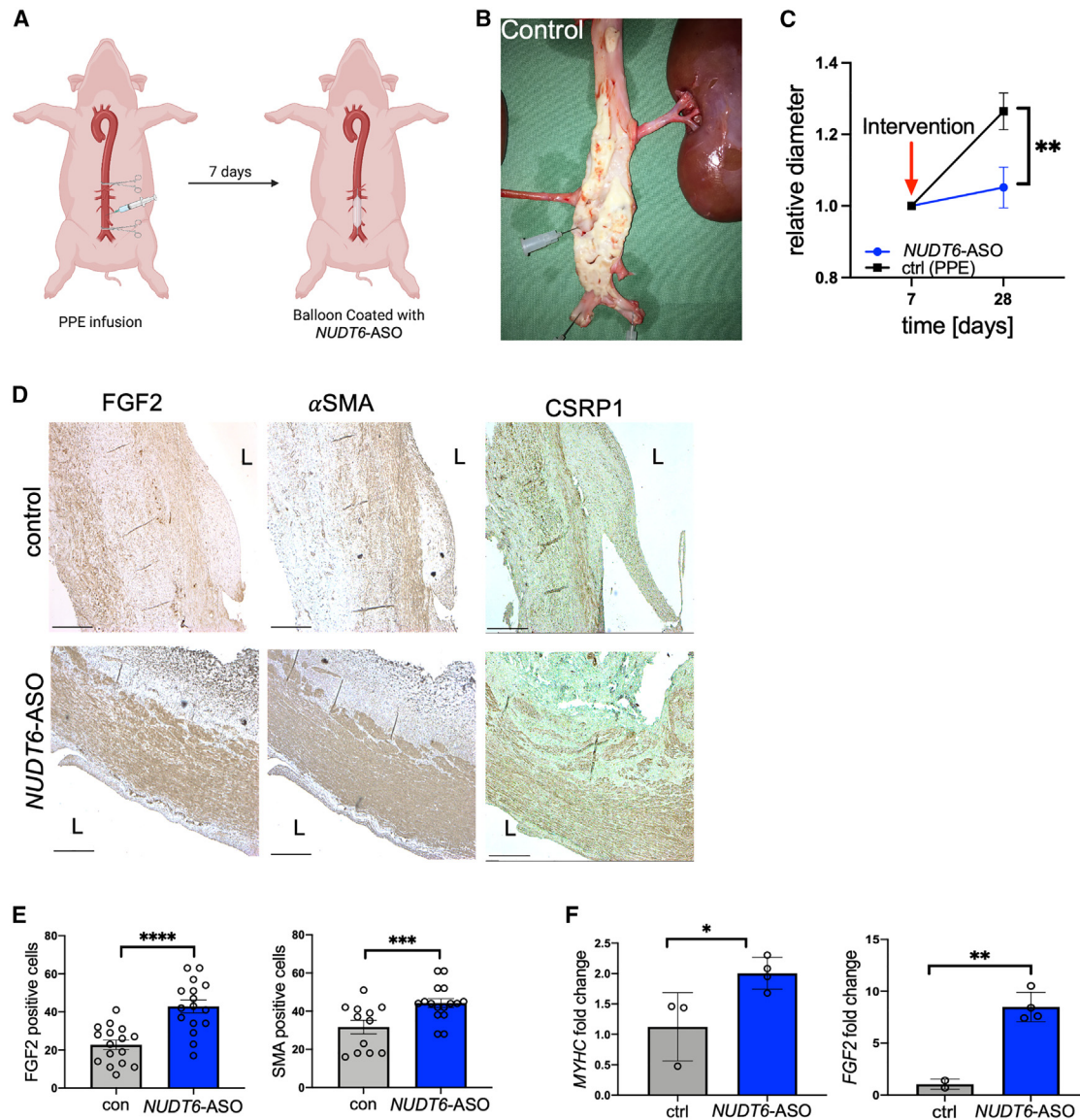


Figure 6. Translational aspects of *NUDT6* inhibition in a large animal model of AAA

(A) Scheme describing the AAA induction in *LDLR*^{-/-} Yucatan minipigs, in which the abdominal aorta was clamped and infused with PPE for 1 min. Seven days later, a balloon coated with *NUDT6*-ASO was introduced via the femoral artery and inflated for 3 min. (B) Representative image of the abdominal aorta of a control *LDLR*^{-/-} minipig. (C) The relative diameter of *NUDT6*-ASO-treated animals ($n = 4$) shows a decrease compared with DEB control-treated animals ($n = 3$). (D) Immunohistochemical staining of the abdominal aorta of control and *NUDT6*-ASO-receiving pigs using antibodies against FGF2, α SMA, and CSRP1. "L" indicates lumen. (E) Quantification (four high-power fields per aorta, in total 16 counts) of immunohistochemical staining from (D) for FGF2 and α SMA. (F and G) qRT-PCR of whole porcine aortic tissue shows a significant increase in MYHC (F) and FGF2 (G) mRNA expression in *NUDT6*-ASO-treated animals ($n = 4$) compared with control ($n = 3$). Quantitative results are presented as mean \pm SEM. * $p < 0.05$, ** $p < 0.01$, *** $p < 0.001$; **** $p < 0.0001$. Significance was determined using two-way ANOVA with Sidak (C) and one-tailed Student's *t* tests (E)–(G). Scale bar, 500 μ m.

to gain insight into the specific cellular expression pattern of our targets. Of importance, *CSRP1* expression seemed mainly restricted to SMCs (Figures 5C, 5D, and S3D) in all three species. This observation was confirmed by IHC staining of human control aorta and AAA, where *CSRP1* levels were reduced in AAA compared with healthy aortic tissue (Figure 5E). Further, significantly lower *CSRP1* mRNA levels were found in AAA (Figure 5F). Of note, both *NUDT6* and

FGF2 were discovered but lowly expressed in the human and porcine scRNA-seq datasets. However, the two transcripts were found to be more highly expressed in murine AAAs (Figure S3E).

We were also able to see a difference in carotid atherosclerotic lesions. Bulk RNA sequencing data of early and advanced lesions (Figure S3F) showed lower *CSRP1* expression in the more diseased state. Also, IHC

of control, stable, unstable, and ruptured carotid lesions indicated decreased expression of CSRPI in the aforementioned order. Interestingly, CSRPI expression in the stable lesion appeared enriched in the fibrous cap, while its expression was lost in unstable or ruptured cap structures (Figure S3G).

To further study the effect of *NUDT6* on CSRPI, we modulated its expression in hAoSMCs using plasmid-based overexpression and GapmeR-mediated knockdown. Overexpression of *NUDT6* substantially downregulated CSRPI (Figure 5G), while inhibition of *NUDT6* increased its protein levels (Figure 5H). This indicates the regulatory function of *NUDT6* on SMC migration, survival, and de-differentiation via targeting of CSRPI.^{37,39} This effect is independent, but additive in vascular disease development, to its antisense regulation of the *FGF2* gene.

***NUDT6* inhibition limits aortic aneurysm development in *LDLR*-deficient Yucatan minipigs**

Finally, we attempted a translational therapeutic intervention in a novel preclinical large animal model of AAA disease, utilizing *LDLR*-deficient Yucatan minipigs. One-year-old male *LDLR*^{-/-} minipigs were fed a high-cholesterol Western diet for 6 months to trigger advanced atherosclerotic disease (Figure S4A). AAAs for this study were induced via catheter-directed PPE infusion into the infrarenal section of the porcine aortas as previously described.^{33,34} Site-specific GapmeRs targeting porcine *NUDT6* were tested in pig fibroblasts before application (Figure S4B) to ensure sufficient knockdown. To potentiate efficient *NUDT6* inhibition and enhance our study's translational feasibility, a local application using drug-eluting balloons (DEBs) coated with *NUDT6*-ASO was chosen. Seven days after AAA induction (mimicking a small but clinically relevant aneurysm in humans), *NUDT6*-ASO was locally applied to target the AAAs via one-time endovascular DEB treatment. A sham intervention was performed using vehicle-only coated DEBs and served as the control group.

From the time of intervention, we realized a significant difference in the relative aortic diameters between the two groups. *NUDT6*-ASO DEB-treated animals displayed significantly smaller diameters than the control group (Figure 6C). Profound changes in *FGF2* and *ACTA2/αSMA* expression on protein and mRNA levels could be observed in the treatment vs. the control group (Figures 6D and 6E). These results were further confirmed on the mRNA level by qRT-PCR (Figures 6F, 6G, and S4C). In addition, expression profiles of the other direct *NUDT6* RNA-protein interaction partner, CSRPI, resembled our *in vitro* results, with increased expression in the aortas from pigs receiving the *NUDT6*-ASO treatment (Figure 6D). The overall aortic morphology, including elastic layer integrity, SMC shape (not spindle-like), and content (yellow staining in Elastica van Giesson indicates SMCs), immune cell infiltrates, and atherosclerotic plaque burden was less altered compared to internal control tissue specimens (Figure S4D).

DISCUSSION

Increasing evidence shows that several non-coding RNA (ncRNA) subclasses (e.g., microRNAs, lncRNAs) play an essential role in medi-

ating gene expression in health and disease. lncRNAs regulate gene expression transcriptionally as well as post-transcriptionally by affecting the stability and translation of protein-coding mRNAs. The numbers of ncRNAs (and possibly their functions) have increased with evolution, perhaps explaining how organisms developed complexity without a corresponding increase in protein-coding genes.⁴⁰ However, it is still being determined how many of these transcripts, particularly those with low abundance, are functional or transcriptional artifacts. Nonetheless, the number of annotated ncRNAs in humans continues to grow and has already surpassed the amount of protein-coding genes by far.

The explosion of new RNA classes has raised the possibility of new therapeutic strategies that mimic or antagonize their function. Attempts to therapeutically target RNA pathways began as soon as they were discovered, even before their mechanism of action had been revealed. On the contrary, within the roughly 20,000 expressed human proteins, only a fraction of 10%–15% are thought to be involved in disease development and exacerbation.⁴¹ Thus, disrupting their activity is likely to have a therapeutic benefit in patients with cardiovascular disease. Most potentially disease-related proteins are termed “undruggable,” implying that they lack distinctive cleft-like motifs into which small molecules can bind with high affinity and specificity.⁴² These “undruggable” proteins contain many transcription and growth factors, as well as epigenetic mediators. In this dilemma, several RNA-based drugs have shown clinical benefits for treating patients with previously considered intractable diseases.⁴³ Most novel drugs that interfere with RNA expression use nucleic acid analogs, taking advantage of complementary base pairing to mimic or antagonize endogenous RNA processes like the GapmeRs (ASOs) utilized in our *in vivo* experiments.

In our present study, we report a substantial imbalance of *NUDT6* and its sense target *FGF2* in the context of two different vascular diseases: advanced atherosclerosis and AAAs. Both diseases share common key features, such as tissue infiltration of inflammatory cells, impaired ECM remodeling, and SMC apoptosis. The latter process is known to further be associated with the thinning of fibrous caps and larger necrotic cores⁴⁴ in carotid artery plaques, while in AAA, SMC apoptosis has been extensively acknowledged as a major process underlying aneurysm formation and progression. In particular, upregulation of *NUDT6* and a concomitant downregulation of *FGF2* mRNA and protein were observed within fibrous caps of vulnerable atherosclerotic human plaques and in aneurysmal aortas from patients undergoing elective open repair surgery. A significant focus of our study was to identify molecular circuits and to develop novel therapies aimed at halting late-stage disease events, such as the destabilization and vulnerability of an advanced plaque and acute rupture of AAA.

One possibility to prevent these events is stabilizing the vessel wall or fibrous cap by re-activating proliferation and migration pathways in de-differentiated/senescent SMCs. We were able to show that de-repression of *FGF2* via inhibiting *NUDT6* in both carotid and aortic

SMCs led to increased proliferation, migration, and decreased apoptosis. In contrast, the opposite could be observed in gain-of-function studies using *NUDT6* overexpression. Upon *NUDT6* targeting, SMCs regained their migratory capacity and contributed to forming a thicker fibrous cap in carotid atherosclerosis. The same was true in dilated aortas, where *NUDT6* inhibition strengthened the weakened vessel wall. The identified protein interaction partner of *NUDT6*, *CSR1*, further points toward a dynamic regulatory role of *NUDT6* in SMCs in health and disease states apart from acting as an antisense to *FGF2*. *CSR1* is a co-activator of the serum response factor, which controls SMC differentiation and proliferation.^{37–39}

It was shown previously that applying basic fibroblast growth factor (bFGF/FGF2) to the abdominal aorta via a biodegradable hydrogel halted aneurysm progression and restored the contractile capacity of SMCs.^{45,46} Also, in intracranial aneurysms, the lncRNA *ANRIL* was shown to influence the proliferation of SMCs by positively regulating FGF2.⁴⁷ However, the role of FGF2 in atherosclerosis is more complex and dynamic: in early stages, it can support macrophage infiltration⁴⁸ while triggering intimal hyperplasia and thickening.⁴⁹ In our experience, using an early-disease mimicking HFD-induced atherogenesis model, we could not detect a change of either *Nudt6* or *Fgf2* in the aortic arches of *ApoE*^{-/-} mice.

It has, however, also been shown that in combination with PDGF-BB, high FGF2 levels can be beneficial by structurally normalizing abnormal neovessels and thereby improving plaque stability.⁵⁰ This is in line with our observations where *FGF2* mRNA expression in micro-dissected fibrous caps was strongly deregulated. In contrast, *FGF2* mRNA from whole carotid plaque tissues did not differ in expression between stable and unstable/ruptured lesions. Thus, it seems to be dependent on the progression of the respective disease to determine when to re-activate FGF2, as well as on the location of the FGF2 signal within the advanced plaque (media, necrotic core, or fibrous cap).

Using GapmeRs targeting *NUDT6* in four different animal models from two different species, we could trigger FGF2 at a late time point of the disease and observed positive effects on rupture rate and abdominal aortic diameter, respectively. Systemic injection of *NUDT6* GapmeR in the murine inducible plaque rupture model and the murine PPE-induced AAA model led to different effects on *NUDT6* mRNA, as well as FGF2 and α SMA protein and mRNA levels. Based on this, the overall composition of the vasculature appeared less diseased and better remodeled. In the murine AngII and the porcine PPE AAA models, we applied *NUDT6* GapmeR locally to the aortic wall using two different methods, which both increase the translational value of utilizing *NUDT6* GapmeRs. UTMD, successfully used for clinical trials in patients with inoperable pancreatic cancer,⁵¹ appears as a feasible and translational approach for delivering ASOs to the abdominal aorta. Interestingly, in patients with pancreatic cancers, the previously deemed “undruggable” transcript *KRAS* was targeted by employing local RNA therapy utilizing a polymeric matrix containing siRNA.^{52,53} These findings pinpoint the ne-

cessity and opportunity of potent local administration of RNA therapeutics, such as siRNAs, ASOs, and antagomiRs.

Based on the idea of enhanced local delivery, we utilized DEBs in male and female *LDLR*^{-/-} Yucatan minipigs in a preclinical AAA model, demonstrating the feasibility of enhanced *NUDT6* inhibition. This is the first study in the cardiovascular field to target an lncRNA with ASOs in a large porcine animal model.⁵⁴ MicroRNAs have been successfully targeted before in large animal models⁵⁴ and are currently being assessed in phase II clinical trials for treatment in patients with myocardial ischemia⁵⁵ and heart failure.⁵⁶ We are convinced that our study provides evidence and hope that inhibition of *NUDT6* presents a novel therapy to limit the burden of atherosclerotic vascular diseases, such as advanced carotid stenosis and AAAs. Future studies will aim at optimizing the local delivery of the *NUDT6*-ASO strategy into carotid plaques and aortic aneurysms to successfully treat our increasing number of patients with both vascular pathologies.

MATERIAL AND METHODS

Patient specimen

The tissue derived from the Munich Vascular Biobank.⁵⁷ Carotid specimens were harvested during carotid endarterectomy, AAA samples were collected during open aneurysm repair and stored in DMEM/F12 medium (Sigma-Aldrich, Darmstadt, Germany) for further processing (see section “[cell culture and transfection](#)” for further details) cell culture purposes. Specimens for staining were fixed in 2% zinc-paraformaldehyde for 48 h followed by paraffin embedding. For characterization based on American Heart Association staging after Stary et al.⁵⁸ as well as fibrous cap thickness after Redgrave et al.,⁵⁹ 5- μ m sections were stained with hematoxylin and eosin (H&E) as well as Elastica van Gieson’s (EvG). For RNA analysis, fresh-frozen specimens stored at -80°C were used.

Laser capture microdissection of fibrous cap tissue derived from advanced atherosclerotic carotid plaques

Human specimens were treated as described in the [supplemental methods](#). Murine specimens were embedded in optimum cutting temperature compound (OCT) medium (Sakura Fine-Tek, Umkirch, Germany) and stored at -80°C until further processing. Before H&E staining, mouse sections were fixed in 4% PFA (Sigma-Aldrich, Darmstadt, Germany) for 10 min. H&E was performed on RNase-free glass slides and pre-treated with UV light at 254 nm for 30 min to promote better adhesion to the slide. Up to 10 consecutive slides per patient were micro-dissected and collected in 350 μ L of RLT buffer (Qiagen). The sample was inverted and centrifuged at 13,000 rpm for 5 min and stored at -80°C . RNA extraction was performed with the RNeasy Micro Kit (Qiagen, Hilden, Germany) after the manufacturer’s instructions. RNA quality was verified using Agilent 2100 Bioanalyzer (Agilent Technologies), and RNA quantity was measured using NanoDrop (Agilent Technologies). For further information, please refer to Jin et al.²⁸

In situ hybridization

Frozen sections were thawed and hybridized with Exiqon miRCURY LNA GapmeR microRNA ISH Optimization Kit (Exiqon, Denmark

or Qiagen, Hilden, Germany) following the instructions of the manufacturer with minor modifications (according to Exiqon's Guidelines for ISH on fresh-frozen material using the miRCURY LNA ISH Optimization kits) and using Pertex (VWR, Stockholm, Sweden) for mounting. Slides were stained for *NUDT6* (562759-2, Exiqon, Denmark). Nuclear counterstaining was done with Nuclear Fast Red (Sigma-Aldrich, Darmstadt, Germany) for 1 min and then washed in 37°C tap water for 10 min before mounting.

Immunohistochemistry

For frozen sections, the following primary abcam antibodies (Cambridge, UK) were used: α -Smooth muscle actin (ab5694), FGF2 (ab8880), Caspase 3 (ab13847), Ki-67(ab16667). As secondary antibody, horseradish peroxidase goat anti-rabbit immunoglobulin (Ig)G (Vector Laboratories, Peterborough, UK) has been used. AEC staining (Histofine Simple Stain, Nichirei Bioscience Inc., Tokyo, Japan) has been performed under surveillance. Counterstaining with Mayer's Hematoxylin (Vector Laboratories, Peterborough, UK) for 10 s has been performed.

For formalin-fixed paraffin-embedded sections, samples were rehydrated, and antigen retrieval was performed in pH 6 in citrate buffer. H₂O₂ blocking was performed prior to primary antibody incubation. For this, the Dako REAL Detection System Peroxidase/DAB+, Rabbit/Mouse Kit (Dako Denmark, Glostrup, Denmark) was used. The following steps were performed after the manufacturer's instructions. Slides were dehydrated in an increasing ethanol row followed by xylene. For mounting, EUKITT (Sigma-Aldrich, Darmstadt, Germany) was used before imaging was performed.

RNA isolation and qRT-PCR

Cells were harvested 24 h after transfection (described above). Homogenization of the cells was achieved by adding 700 μ L QIAzol (Qiagen, Hilden, Germany) to the cells, scraping them off with a cell scraper (Sigma-Aldrich) and pipetting up and down three times. Tissues were lysed in 1 mL QIAzol with a tissue homogenizer (ProScientific, Oxford, MS, USA). RNA isolation was performed with miRNeasy MiniKit (Qiagen, Hilden, Germany) following the instructions given by the provider. RNA concentration was measured using a NanoDrop 2000 spectrophotometer (Thermo Fisher Scientific, Gothenburg, Sweden). cDNA was synthesized with the cDNA RT kit (Applied Biosystems, Foster City, CA, USA) according to the manufacturer's protocol using 10 ng of RNA. TaqMan qRT-PCR assay was performed for *NUDT6* and *FGF2* (Thermo Fisher Scientific, Gothenburg, Sweden) using 300–400 ng of cDNA. Housekeeping control ACTB (Thermo Fisher Scientific, Gothenburg, Sweden) was used to normalize the assays. $\Delta\Delta$ Ct was calculated in Excel to determine the fold change. For more information about the used primers, see the Appendix.

Mouse carotid plaque rupture model

Via incision of the medial neck, the right carotid artery of an *ApoE*-deficient mouse was cleared from connective tissue. A 5.0 VICRYL suture (Ethicon, Johnson & Johnson AB, Sollentuna, Sweden) was

placed around the carotid artery below the bifurcation following the closure of the skin with 5.9 VICRYL suture (Ethicon, Norderstedt, Germany). Twenty-eight days afterward, a 1.77-mm-long plastic cast consisting of two-halves (Promolding BV, Rijswijk, Netherlands) with a triangular-shaped internal lumen ranging from 150 μ m (distal) to 300 μ m (proximal) was placed proximal to the ligation around the carotid artery. Before that, flow through the ligated part of the carotid artery was verified by Doppler-enhanced ultrasonography (Vevo 2100, VisualSonics, Toronto, Canada). After the cast was placed, animals were killed, and organs were harvested.

Mouse Angiotensin II-induced AAA model

Once they reached the age of 10 weeks, osmotic minipumps (model 2004, Alzet, Cupertino, CA, USA) with Ang II (Sigma-Aldrich, Stockholm, Sweden) were implanted subcutaneously into the back/neck area of the anesthetized (2.0% Isoflurane-containing oxygenated air) *ApoE*-deficient mouse on day 1. A steady delivery of 1,000 ng/kg/min was thereby ensured. Determination of the aortic diameter via ultrasound (VisualSonics; Vevo 2100 Imaging System) was performed at baseline, and then after 7, 14, and 28 days. In addition, the aortic wall was examined for potential dilations and lesions on days 7, 14, and 28. Mice were anesthetized prior to ultrasound with Isoflurane (Santa Cruz Biotechnology, Dallas, TX, USA).

UTMD-mediated local aortic *Nudt6* GapmeR delivery

The procedure was performed as recently described by Jin et al.²⁸ In brief, mice subjected to Angiotensin II osmotic minipumps received 200 μ L cationic microbubbles (SonoVue), which were charge-coupled to *Nudt6* GapmeR or an FAM-labeled scrambled control (Qiagen, Hilden, Germany). Mice were anesthetized after aortic diameter measurement, and a phased transducer (Sonitron GTS Sonoporation System) was placed on the abdominal aorta, which was marked with a pen according to the localization of the infrarenal aorta. For 15 min, ultrasound was transmitted with 1 MHz, 2.0 w/cm², and 50% duty cycles.

Mouse porcine pancreatic elastase-induced AAA model

The proximal and distal aorta of anesthetized (2.0% Isoflurane-containing oxygenated air) C57BL/6J mice was temporarily ligated at the proximal and distal end. An incision at the bifurcation and an infusion catheter was used for flushing the aorta for 5 min at 100 mm Hg with saline or saline-containing type I PPE (1.5 U/mL; Sigma-Aldrich, Darmstadt, Germany). Then, the catheter was removed, and the incision was closed with a suture without constricting the aortic lumen. The aortic diameter was measured, as explained in the previous paragraph.

In vivo *Nudt6* inhibition

Ten milligrams per kilogram fluorescently labeled scrambled control oligonucleotide or *NUDT6* specific GapmeR inhibitor (*NUDT6_6* GGACCTGAATTCTGA, Exiqon, Vedbaek, Denmark) was injected intraperitoneally. For the carotid artery atherosclerotic model, mice received a four-time injection on days 1, 11, 21, and 28. For the AngII mouse model, mice received three-time injection on days 1,

11, and 21, followed by the described UTMD procedure. On day 28, the mice were killed through CO₂ inhalation, exsanguinated by heart puncturing, and perfused with PBS. For the PPE mouse model, mice received a one-time intraperitoneal injection after surgery on the same day. Organs were snap-frozen in dry ice and stored at -80°C . The aneurysmal aorta and the common right carotid artery were embedded into OCT (Histolab, Gothenburg, Sweden), snap-frozen, and stored at -80°C for sectioning.

Cell culture and transfection

Primary mouse aortic smooth muscle cells (mAoSMC), grown in DMEM/F12 (Gibco, Thermo Scientific, Gothenburg, Sweden) supplemented with 10% FBS (Gibco, Thermo Scientific, Gothenburg, Sweden) and 1% Penicillin-Streptomycin (PeSt) or human aortic/carotid smooth muscle cells (hAoSMC; hCtSMC), grown in SMC Growth Medium (PELO Biotech, Martinsried, Germany) were passaged up to five to six times and seeded at 100,000 cells/well (six-well plate) or 10–15,000 cells/well (48-well plate).

Patient-derived cells from aneurysmatic or atherosclerotic tissue samples were collected during open AAA repair or carotid endarterectomy (CEA) and stored short-term in DMEM (Gibco, Thermo Scientific, Darmstadt, Germany) at $+4^{\circ}\text{C}$. Then, the adventitia and, if possible, the endothelium was removed and the tissue was incubated at 37°C , 5% CO₂ on collagen-coated petridishes in SMC Growth Medium. Cells were used until passage seven.

Pig fibroblasts were provided by Associate Professor Yonglun Luo from Aarhus University, Denmark, and derived from Yucatan minipigs.

NUDT6 gene silencing and overexpression in hCtSMC and hAoSMCs were performed using Silencer Select Negative Control No. 1 siRNA (Ambion Life Technologies Corp., Carlsbad, CA, USA), *NUDT6* siRNA (Ambion Life Technologies Corp., Carlsbad, CA, USA), pCMV6-Entry Tagged Cloning Vector (OriGene Technologies, Inc., Rockville, MD, USA), and *NUDT6* Human Tagged ORF Clone plasmid (OriGene Technologies, Inc., Rockville, MD, USA) according to the manufacturer's standard protocols. Lipofectamine RNAiMAX (Life Technologies Corp., Carlsbad, CA, USA) and Lipofectamine 3000 (Life Technologies Corp., Carlsbad, CA, USA) were used as transfection reagents. To further verify the effects of *NUDT6* protein on hCtSMCs, *NUDT6* peptides were transfected with Pierce Protein Transfection Kit (Thermo Scientific Pierce RIPA Buffer, Thermo Scientific, Waltham, MA, USA) according to the company's protocol. Pierce β -Galactosidase Control and Pierce FITC-Antibody Control in the transfection kit were used as control peptides for the experiment.

To further characterize the mechanism underlying enhanced *NUDT6*, cells were treated with 0.5 nM AngII (Sigma-Aldrich, Darmstadt, Germany), 20 $\mu\text{g}/\text{mL}$ oxLDL (kindly provided by Eva Ehrenborg Group, Karolinska Institutet, Solna, Sweden) in Optimem (Gibco, Thermo Scientific, Darmstadt, Germany) supplied with 10% FBS, only Opti-

mem supplied with 10% FBS, or Optimem supplied with 2% FBS as starvation group. RNA was isolated (see below) after 24 h of treatment and kept at -80°C .

Cell proliferation, migration, and apoptosis assay using IncuCyte ZOOM

Minimum 6–8 h after transfection, cells were live imaged with the IncuCyte imaging system (IncuCyte, Essen Bioscience, Hertfordshire, UK). The experiment was conducted for 24–72 h, repeated at least two times with triplicates of each group for statistics. To identify the effect of *Nudt6* modulation and its peptides on human carotid SMCs and human aortic smooth muscles, cell proliferation (confluence), migration, and apoptosis assays were performed and analyzed by IncuCyte Live Cell Analysis System (Sartorius Stedim Plastics GmbH, Goettingen, Germany) under *Nudt6* modulation (overexpression or silencing). IncuCyte Caspase-3/7 Apoptosis Assay Reagent (Sartorius Stedim Plastics GmbH, Goettingen, Germany) was used to detect apoptotic cells following the manufacturer's protocol.

Protein extraction and western blotting

hCtSMCs or hAoSMCs were washed with PBS and resuspended in protein isolation buffer. Protein was then extracted for 30 min at 4°C in a rotating mixer and quantified by using Pierce BCA Protein Assay Kit (Thermo Scientific, Waltham, MA, USA). Ten micrograms of protein from each lysate were separated by 12% Mini-PROTEAN TGX Stain-Free Protein Gels (Bio-Rad Laboratories AB, Solna, Sweden) in SDS-PAGE buffer in Mini-PROTEAN Tetra Vertical Electrophoresis Cell (Bio-Rad Laboratories AB, Solna, Sweden). Gel was then transferred to a Trans-Blot Turbo Mini polyvinylidene difluoride (PVDF) Transfer membrane (Bio-Rad Laboratories AB, Solna, Sweden) by using the Trans-Blot Turbo Transfer System (Bio-Rad Laboratories AB, Solna, Sweden), followed by blocking the membrane with 5% skim milk (Bio-Rad Laboratories AB, Solna, Sweden) (hCtSMCs) or 5% BSA (Sigma-Aldrich) in TBS-T. Immunodetection of FGF2 and β -actin on membrane was performed through conjugated secondary antibodies to primer antibodies. Membrane was finally incubated in AmerSham ECL Prime western blotting detection reagent (GE Healthcare UK Ltd., Buckinghamshire, UK) for 5 min and exposed by CCD camera.

scRNA-seq data analysis

The scRNA-seq datasets were analyzed with Seurat (version 4.1.0) in R (version 4.1.1).^{60,61} CellCycleScoring function⁶² in Seurat was applied to calculate the scores of cell cycle phases like S phase and G2M phase. SCTransform normalization workflow⁶³ was adopted to mitigate possible technically driven or other variations in which mitochondrial genes and cell cycle phase were regressed out. In the human dataset, a total of 3,000 cells were used for the downstream analysis. In the pig models, 6,899 cells passed the quality control and were included for analysis, while 13,002 cells were analyzed in the mice models. T-SNE (t-Distributed Stochastic Neighbor Embedding) was used for converting cells into two-dimensional maps. FindAllmarkers function was performed to detect the main features

of each cluster with default parameters. The top expressed genes were mainly used for the consideration of cell-type identifications.

RNA pulldown

For linearization, 2.5 µg NUDT6 Human Tagged ORF Clone (OriGene Technologies, Inc. Rockville, MD, USA) or GFP plasmid, respectively, were digested with XhoI for 1 h (New England Biolabs, Ipswich, MA, USA). Both constructs were run on a 1% agarose gel to check for complete linearization. PCR cleanup kit (Qiagen, Hilden, Germany) was used to purify the DNA, which NanoDrop then measured. Next, T7 polymerase (Promega, Walldorf, Germany), as well as the Roche Biotin RNA labeling kit (Sigma-Aldrich, Darmstadt, Germany), was used for *in vitro* transcription (IVT) of 1 µg linearized constructs. After that, TURBO DNase (Invitrogen, Darmstadt, Germany) was used to remove the template from the reaction. QuickSpin Sephadex columns (Roche, Sigma-Aldrich, Darmstadt, Germany) were used to remove any unwanted leftovers from IVT. The size and integrity of the biotinylated RNA were checked on a 6% urea gel (Thermo Scientific, Darmstadt, Germany). Immediately before use, the RNA was heated to 95°C for 2 min, on ice for 3 min, and left at room temperature for 25 min in RNA folding buffer (20 mM Tris-HCl pH 7.5, 100 mM KCl, 10 mM MgCl₂, 20 U RNase OUT) to ensure correct folding. For each pulldown reaction, 1.5 M hAoSMCs p6/p7 was used. Cells were washed twice with PBS before collection. After another wash, cells were lysed in lysis buffer (50 mM Tris-HCl pH 8, 150 mM NaCl, 0.5% [v/v] NP40, 1x Roche cOmplete protease inhibitor, 20 U RNaseOUT) for 30 min followed by a full-speed 30-min centrifugation. The supernatant was diluted in dilution buffer (20 mM Tris-HCl pH 7.4, 150 mM NaCl, 2 mM EDTA pH 8.0, 0.5% Triton X, and freshly added RNaseOUT and 2x Roche cOmplete protease inhibitor) and a pre-clearing step with washed MyC1 streptavidin beads (Invitrogen, Darmstadt, Germany) was performed. Beads were removed and a 5% Input sample was taken for control purposes; 250 ng of biotinylated IVT NUDT6 (or GFP, as a control reaction) was incubated with pre-cleared cell lysate on an overhead shaker at 4°C overnight. On the next day, the streptavidin beads were added to the samples for 3 h on an overhead shaker at 4°C. Bead-target complexes were washed 3x in dilution buffer on the shaker at 4°C followed by one wash with 200 mM NaCl dilution buffer. For LC-MS analysis, samples were washed briefly in M/S buffer (10 mM Tris-HCl pH 7.4, 150 mM NaCl). To control the efficiency of the pulldown, both qRT-PCR and silver staining was performed.

Liquid chromatography-mass spectrometry

Mass spectrometry data, together with a detailed description of methods and data analysis, have been deposited to the ProteomeXchange Consortium via the PRIDE partner repository⁶⁴ with the dataset identifier PXD033922.

RNA immunoprecipitation

The Magna RIP 17-700 Kit (Millipore, Burlington, MA, USA) was used together with a polyclonal CRP1 antibody (PA5-86703, Invitrogen, Thermo Scientific, Darmstadt, Germany) to perform the

RNA immunoprecipitation according to the manufacturer's instructions. Briefly, hAoSMCs were grown in T175 flasks (1 flask per reaction and per analysis), washed with PBS, and lysed in the provided RIP lysis buffer (Millipore, Burlington, MA, USA) according to the protocol. The lysate was spun down at 12,000 rpm, and the supernatant was divided into 20% input and two reactions, CRP1 and IgG control. The supernatant was applied to the respective antibody-pre-incubated magnetic beads (5 µg antibody per reaction). The provided rabbit IgG antibody was used as a control (Millipore, Burlington, MA, USA). After overnight incubation at 4°C, the reaction was washed 6x at 4°C before elution. The eluate as well as beads, input, and first wash supernatant were subjected to RNA and protein analysis.

Porcine *in vivo* study

Eight female and castrated male LDLR^{-/-} Yucatan minipigs (Exemplar Genetics, Coralville, IA, USA) were acclimatized prior to surgery under conventional hygienic standards and received water *ad libitum* and pelleted HFD (Altromin, Lage, Germany).

PPE procedure

On day 0, ultrasound and AAA induction by PPE procedure was performed, on day 8—after ultrasound measurement—the aorta was treated with an endovascular balloon. On day 28, another ultrasound followed by euthanasia and tissue collection was performed.

Prior to anesthesia, the animal was sedated (15 mg/kg ketamine, 2 mg/kg azaperone, 0.1 mg/kg atropine) intramuscularly. Then, an intravenous catheter was placed and the anesthesia was induced with 4–8 mg/kg propofol. The animal was intubated (7–8.5 mm cuffed endotracheal tube) and anesthesia was maintained by continuously infusing 2.5–7 mg/kg/h propofol. Before skin incision, cefuroxime (750 mg) was administered and further analgesia was maintained throughout the surgery (50 mg/kg metamizole, 4 mg/kg carprofen, 0.001–0.01 mg/kg fentanyl).

All ultrasounds were performed using a GE logiq S7 system (GE, Frankfurt, Germany) by two independent examiners. For orientation, the renal arteries and trifurcation were identified. Then, the aortic diameter was measured using leading edge technique in transverse and longitudinal sections at the point of maximum diameter.

The PPE procedure was performed via the left lateral flank. The aorta was isolated from the left renal artery to the aortic trifurcation. Lumbar arteries were clipped. Prior to aortic clamping, 3,000 IU heparin was given. Depending on the measured aortic diameter, a 9–11 × 20 mm PTA balloon (Medtronic Admiral Xtreme) was inserted and inflated to 10 atm for 1 min to secure pre-dilation of the aorta. By inserting a blunt needle (5G) into the aorta, the elastase perfusion (10 IU/mL, PPE, Sigma-Aldrich, Germany) could be performed for 10 min using a pressure syringe. Then, the aorta was flushed with saline followed by closure of the aorta with a 5-0 suture. Closure of muscle, fat, and skin layers was done and the wound was finally coated with a spray on dressing (Aqueous UK) to prevent infection.

Balloon treatment

The *NUDT6* GapmeR was prepared in a 33-mM dilution (Qiagen, Hilden, Germany), spray coated on a 10–12 × 20-mm PTA balloon (Medtronic Admiral Xtreme) and introduced via the femoral artery advancing to the aneurysm, which was identified via angiogram. The balloon then was inflated to 10 atm for 3 min. To exclude aortic occlusion or dissection, an angiography was performed.

Analgesia, blood sampling, euthanasia

Toward the end of anesthesia, buprenorphine (0.005–0.01 mg/kg) was administered. In the case of PPE procedure, administration was continued for at least 2 days. After the surgery, carprofen (4 mg/kg) was administered orally for at least 5 days.

Blood sampling was performed at day 0, 8 (±2), and 28 (±3) under anesthesia.

On day 28, animals were killed after a final aortic ultrasound using pentobarbital (>50 mg/kg) and 40 mL of 1 M KCl solution.

Statistics

Quantitative data are shown as dot plots with columns representing the mean and with error bars representing the SEM. Repetitive data are shown as dots representing the mean and with error bars representing the SEM connected by lines. Continuous variables between two groups were done by Student's *t* test. More than two groups were analyzed by one-way ANOVA or two-way ANOVA, depending on the number of independent variables. For repeated measures over time, multiple *t* tests were used. *p* < 0.05 was used to show statistical significance with probability values two-tailed or one-tailed as indicated.

Statistical analyses and graphs were generated with GraphPad Prism 8 or newer.

Study approval

All patients provided written and informed consent according to the Declaration of Helsinki. The study was approved by the local ethics committee (protocol No. 2799/10 and 2799/10S).

Male *ApoE*^{−/−} mice (Taconic Biosciences, Hudson, NY, USA) and C57BL/6J mice (The Jackson Laboratory, Bar Harbor, ME, USA) were maintained in the local animal facility under ethical approval of the local ethics committee (Swedish Board for Agriculture; Ethical permit no. N48/16). The mice had *ad libitum* access to water and a standard chow diet. The animal study using minipigs was approved by the Animal Ethical Committee of the Government of Upper Bavaria (Munich, Germany; protocol No. ROB-55.2-2532.Vet_02-18-53) and performed in accordance with respective guidelines (EU Directive 2010/62/EU and Animal Welfare Act (2018)).

DATA AVAILABILITY

All data presented in this manuscript are either displayed in the results or online supplement. Additional data can be provided upon reasonable request to the corresponding author.

SUPPLEMENTAL INFORMATION

Supplemental information can be found online at <https://doi.org/10.1016/j.ymthe.2023.04.020>.

ACKNOWLEDGMENTS

The authors thank Marie-Luise Engl, Nadiya Glukha, Renate Hegenloh, and Changyan Sun for their technical assistance.

This study is supported (all to L.M.) by the European Research Council (ERC-CoG project LongTx under the grant agreement number 101088370), a DZHK Translational Research Project (TRP), the SFB1123 and TRR267 of the German Research Council (DFG), the National Institutes of Health (NIH; 1R01HL150359-01), the Bavarian State Ministry of Health and Care through the research project DigiMed Bayern, as well as Vetenskapsrådet (2019-01577), and Hjärt-Lungfonden (20210450). B.B.K. acknowledges funding support from Indiana University and NIH R01DK132090.

AUTHOR CONTRIBUTIONS

H.W., F.F., H.J., and L.M. designed the research studies. H.W., G.W., A. Busch, E.C., F.F., A. Bäcklund, and H.J. performed the experiments. Z.W., B.B.K., D.J.v.B., and I.W. acquired data. G.W., Z.W., B.B.K., D.J.v.B., I.W., and R.B. analyzed data and helped with data interpretation. N.S. and H.H.E. provided resources in the form of human specimens. H.W., H.J., and L.M. wrote the original draft of the manuscript. All authors reviewed and edited the manuscript.

DECLARATION OF INTERESTS

L.M. is a scientific consultant and adviser for Novo Nordisk (Malov, Denmark), DrugFarm (Shanghai, China), and Angiolutions (Hannover, Germany), and received research funds from Roche Diagnostics (Rotkreuz, Switzerland) and Novo Nordisk (Malov, Denmark).

REFERENCES

1. GBD 2017 Causes of Death Collaborators (2018). Global, regional, and national age-sex-specific mortality for 282 causes of death in 195 countries and territories, 1980–2017: a systematic analysis for the Global Burden of Disease Study 2017. *Lancet* 392, 1736–1788. [https://doi.org/10.1016/S0140-6736\(18\)32203-7](https://doi.org/10.1016/S0140-6736(18)32203-7).
2. Franck, G., Dai, J., Fife, A., Ngo, S., Justine, C., Michineau, S., Allaire, E., and Gervais, M. (2013). Reestablishment of the endothelial lining by endothelial cell therapy stabilizes experimental abdominal aortic aneurysms. *Circulation* 127, 1877–1887. <https://doi.org/10.1161/CIRCULATIONAHA.113.001677>.
3. Davignon, J., and Ganz, P. (2004). Role of endothelial dysfunction in atherosclerosis. *Circulation* 109, III27–32. <https://doi.org/10.1161/01.CIR.0000131515.03336.f8>.
4. Golledge, J., and Norman, P.E. (2010). Atherosclerosis and abdominal aortic aneurysm: cause, response, or common risk factors? *Arterioscler. Thromb. Vasc. Biol.* 30, 1075–1077. <https://doi.org/10.1161/ATVBAHA.110.206573>.
5. Ailawadi, G., Eliason, J.L., and Upchurch, G.R., Jr. (2003). Current concepts in the pathogenesis of abdominal aortic aneurysm. *J. Vasc. Surg.* 38, 584–588. [https://doi.org/10.1016/s0741-5214\(03\)00324-0](https://doi.org/10.1016/s0741-5214(03)00324-0).
6. Bennett, M.R., Sinha, S., and Owens, G.K. (2016). Vascular smooth muscle cells in atherosclerosis. *Circ. Res.* 118, 692–702. <https://doi.org/10.1161/CIRCRESAHA.115.306361>.
7. Ailawadi, G., Moehle, C.W., Pei, H., Walton, S.P., Yang, Z., Kron, I.L., Lau, C.L., and Owens, G.K. (2009). Smooth muscle phenotypic modulation is an early event in aortic aneurysms. *J. Thorac. Cardiovasc. Surg.* 138, 1392–1399. <https://doi.org/10.1016/j.jtcvs.2009.07.075>.

8. Peshkova, I.O., Schaefer, G., and Koltsova, E.K. (2016). Atherosclerosis and aortic aneurysm - is inflammation a common denominator? *FEBS J.* 283, 1636–1652. <https://doi.org/10.1111/febs.13634>.
9. Sakalihasan, N., Michel, J.B., Katsargyris, A., Kuivaniemi, H., Defraigne, J.O., Nchimi, A., Powell, J.T., Yoshimura, K., and Hultgren, R. (2018). Abdominal aortic aneurysms. *Nat. Rev. Dis. Primers* 4, 34. <https://doi.org/10.1038/s41572-018-0030-7>.
10. Lindholt, J.S., Sogaard, R., and Laustsen, J. (2012). Prognosis of ruptured abdominal aortic aneurysms in Denmark from 1994–2008. *Clin. Epidemiol.* 4, 111–113. <https://doi.org/10.2147/CLEP.S31098>.
11. Karthikesalingam, A., Holt, P.J., Vidal-Diez, A., Ozdemir, B.A., Poloniecki, J.D., Hinchliffe, R.J., and Thompson, M.M. (2014). Mortality from ruptured abdominal aortic aneurysms: clinical lessons from a comparison of outcomes in England and the USA. *Lancet* 383, 963–969. [https://doi.org/10.1016/S0140-6736\(14\)60109-4](https://doi.org/10.1016/S0140-6736(14)60109-4).
12. Nighoghossian, N., Derex, L., and Douek, P. (2005). The vulnerable carotid artery plaque: current imaging methods and new perspectives. *Stroke* 36, 2764–2772. <https://doi.org/10.1161/01.STR.0000190895.51934.43>.
13. Forsdahl, S.H., Singh, K., Solberg, S., and Jacobsen, B.K. (2009). Risk factors for abdominal aortic aneurysms: a 7-year prospective study: the Tromsø Study, 1994–2001. *Circulation* 119, 2202–2208. <https://doi.org/10.1161/CIRCULATIONAHA.108.817619>.
14. Kertai, M.D., Boersma, E., Westerhout, C.M., van Domburg, R., Klein, J., Bax, J.J., van Urk, H., and Poldermans, D. (2004). Association between long-term statin use and mortality after successful abdominal aortic aneurysm surgery. *Am. J. Med.* 116, 96–103. <https://doi.org/10.1016/j.amjmed.2003.08.029>.
15. Wanhainen, A., Verzini, F., Van Herzele, I., Allaire, E., Bown, M., Cohnert, T., Dick, F., van Herwaarden, J., Karkos, C., Koelemay, M., et al. (2019). Editor's choice - European society for vascular surgery (ESVS) 2019 clinical practice guidelines on the management of abdominal Aorto-iliac artery aneurysms. *Eur. J. Vasc. Endovasc. Surg.* 57, 8–93. <https://doi.org/10.1016/j.ejvs.2018.09.020>.
16. Michel, J.B., Jondeau, G., and Milewicz, D.M. (2018). From genetics to response to injury: vascular smooth muscle cells in aneurysms and dissections of the ascending aorta. *Cardiovasc. Res.* 114, 578–589. <https://doi.org/10.1093/cvr/cvy006>.
17. Eken, S.M., Jin, H., Chernogubova, E., Li, Y., Simon, N., Sun, C., Korzunowicz, G., Busch, A., Bäcklund, A., Österholm, C., et al. (2017). MicroRNA-210 enhances fibrous cap stability in advanced atherosclerotic lesions. *Circ. Res.* 120, 633–644. <https://doi.org/10.1161/CIRCRESAHA.116.309318>.
18. Quintana, R.A., and Taylor, W.R. (2019). Cellular mechanisms of aortic aneurysm formation. *Circ. Res.* 124, 607–618. <https://doi.org/10.1161/CIRCRESAHA.118.313187>.
19. Libby, P. (2008). The molecular mechanisms of the thrombotic complications of atherosclerosis. *J. Intern. Med.* 263, 517–527. <https://doi.org/10.1111/j.1365-2796.2008.01965.x>.
20. St Laurent, G., Wahlestedt, C., and Kapranov, P. (2015). The Landscape of long non-coding RNA classification. *Trends Genet.* 31, 239–251. <https://doi.org/10.1016/j.tig.2015.03.007>.
21. Lapidot, M., and Pilpel, Y. (2006). Genome-wide natural antisense transcription: coupling its regulation to its different regulatory mechanisms. *EMBO Rep.* 7, 1216–1222. <https://doi.org/10.1038/sj.embor.7400857>.
22. Darnell, J.E., Jr. (2002). Transcription factors as targets for cancer therapy. *Nat. Rev. Cancer* 2, 740–749. <https://doi.org/10.1038/nrc906>.
23. Lazo, J.S., and Sharlow, E.R. (2016). Drugging undruggable molecular cancer targets. *Annu. Rev. Pharmacol. Toxicol.* 56, 23–40. <https://doi.org/10.1146/annurev-pharmtox-010715-103440>.
24. Pelechano, V., and Steinmetz, L.M. (2013). Gene regulation by antisense transcription. *Nat. Rev. Genet.* 14, 880–893. <https://doi.org/10.1038/nrg3594>.
25. Shimoni, Y., Friedlander, G., Hetzroni, G., Niv, G., Altuvia, S., Biham, O., and Margalit, H. (2007). Regulation of gene expression by small non-coding RNAs: a quantitative view. *Mol. Syst. Biol.* 3, 138. <https://doi.org/10.1038/msb4100181>.
26. Fasolo, F., Jin, H., Winski, G., Chernogubova, E., Pauli, J., Winter, H., Li, D.Y., Glukha, N., Bauer, S., Metschl, S., et al. (2021). Long noncoding RNA MIAT controls advanced atherosclerotic lesion formation and plaque destabilization. *Circulation* 144, 1567–1583. <https://doi.org/10.1161/CIRCULATIONAHA.120.052023>.
27. Tsantilas, P., Lao, S., Wu, Z., Eberhard, A., Winski, G., Vaerst, M., Nanda, V., Wang, Y., Kojima, Y., Ye, J., et al. (2021). Chitinase 3 like 1 is a regulator of smooth muscle cell physiology and atherosclerotic lesion stability. *Cardiovasc. Res.* 117, 2767–2780. <https://doi.org/10.1093/cvr/cvab014>.
28. Jin, H., Li, D.Y., Chernogubova, E., Sun, C., Busch, A., Eken, S.M., Saliba-Gustafsson, P., Winter, H., Winski, G., Raaz, U., et al. (2018). Local delivery of miR-21 stabilizes fibrous caps in vulnerable atherosclerotic lesions. *Mol. Ther.* 26, 1040–1055. <https://doi.org/10.1016/j.ymthe.2018.01.011>.
29. McEachern, L.A., and Murphy, P.R. (2014). Chromatin-remodeling factors mediate the balance of sense-antisense transcription at the FGF2 locus. *Mol. Endocrinol.* 28, 477–489. <https://doi.org/10.1210/me.2013-1220>.
30. Zhang, S.C., MacDonald, K.A., Baguma-Nibasheka, M., Geldenhuys, L., Casson, A.G., and Murphy, P.R. (2008). Alternative splicing and differential subcellular localization of the rat FGF antisense gene product. *BMC Mol. Biol.* 9, 10. <https://doi.org/10.1186/1471-2199-9-10>.
31. Daugherty, A., and Cassis, L. (1999). Chronic angiotensin II infusion promotes atherogenesis in low density lipoprotein receptor -/- mice. *Ann. N. Y. Acad. Sci.* 892, 108–118. <https://doi.org/10.1111/j.1749-6632.1999.tb07789.x>.
32. Berliner, J.A., Leitinger, N., and Tsimikas, S. (2009). The role of oxidized phospholipids in atherosclerosis. *J. Lipid Res.* 50 (Suppl), S207–S212. <https://doi.org/10.1194/jlr.R800074-JLR200>.
33. Li, D.Y., Busch, A., Jin, H., Chernogubova, E., Pelisek, J., Karlsson, J., Sennblad, B., Liu, S., Lao, S., Hofmann, P., et al. (2018). H19 induces abdominal aortic aneurysm development and progression. *Circulation* 138, 1551–1568. <https://doi.org/10.1161/CIRCULATIONAHA.117.032184>.
34. Busch, A., Pauli, J., Winski, G., Bleichert, S., Chernogubova, E., Metschl, S., Winter, H., Trenner, M., Wiegand, A., Otto, C., et al. (2021). Lenvatinib halts aortic aneurysm growth by restoring smooth muscle cell contractility. *JCI Insight* 6, e140364. <https://doi.org/10.1172/jci.insight.140364>.
35. Li, A.W., Too, C.K., and Murphy, P.R. (1996). The basic fibroblast growth factor (FGF-2) antisense RNA (GFG) is translated into a MutT-related protein in vivo. *Biochem. Biophys. Res. Commun.* 223, 19–23. <https://doi.org/10.1006/bbrc.1996.0839>.
36. Asa, S.L., Ramyar, L., Murphy, P.R., Li, A.W., and Ezzat, S. (2001). The endogenous fibroblast growth factor-2 antisense gene product regulates pituitary cell growth and hormone production. *Mol. Endocrinol.* 15, 589–599. <https://doi.org/10.1210/mend.15.4.0626>.
37. Chang, D.F., Belaguli, N.S., Iyer, D., Roberts, W.B., Wu, S.P., Dong, X.R., Marx, J.G., Moore, M.S., Beckerle, M.C., Majesky, M.W., and Schwartz, R.J. (2003). Cysteine-rich LIM-only proteins CRP1 and CRP2 are potent smooth muscle differentiation cofactors. *Dev. Cell* 4, 107–118. [https://doi.org/10.1016/s1534-5807\(02\)00396-9](https://doi.org/10.1016/s1534-5807(02)00396-9).
38. Henderson, J.R., Macalma, T., Brown, D., Richardson, J.A., Olson, E.N., and Beckerle, M.C. (1999). The LIM protein, CRP1, is a smooth muscle marker. *Dev. Dyn.* 214, 229–238. [https://doi.org/10.1002/\(SICI\)1097-0177\(199903\)214:3<229::AID-AJA6>3.0.CO;2-S](https://doi.org/10.1002/(SICI)1097-0177(199903)214:3<229::AID-AJA6>3.0.CO;2-S).
39. Lilly, B., Olson, E.N., and Beckerle, M.C. (2001). Identification of a CArG box-dependent enhancer within the cysteine-rich protein 1 gene that directs expression in arterial but not venous or visceral smooth muscle cells. *Dev. Biol.* 240, 531–547. <https://doi.org/10.1006/dbio.2001.0507>.
40. Deveson, I.W., Hardwick, S.A., Mercer, T.R., and Mattick, J.S. (2017). The dimensions, dynamics, and relevance of the mammalian noncoding transcriptome. *Trends Genet.* 33, 464–478. <https://doi.org/10.1016/j.tig.2017.04.004>.
41. Damase, T.R., Sukhovshin, R., Boada, C., Taraballi, F., Pettigrew, R.I., and Cooke, J.P. (2021). The limitless future of RNA therapeutics. *Front. Bioeng. Biotechnol.* 9, 628137. <https://doi.org/10.3389/fbioe.2021.628137>.
42. Hambly, K., Danzer, J., Muskal, S., and Debe, D.A. (2006). Interrogating the druggable genome with structural informatics. *Mol. Divers.* 10, 273–281. <https://doi.org/10.1007/s11030-006-9035-3>.
43. Warner, K.D., Hajdin, C.E., and Weeks, K.M. (2018). Principles for targeting RNA with drug-like small molecules. *Nat. Rev. Drug Discov.* 17, 547–558. <https://doi.org/10.1038/nrd.2018.93>.
44. Clarke, M.C.H., Littlewood, T.D., Figg, N., Maguire, J.J., Davenport, A.P., Goddard, M., and Bennett, M.R. (2008). Chronic apoptosis of vascular smooth muscle cells

- accelerates atherosclerosis and promotes calcification and medial degeneration. *Circ. Res.* 102, 1529–1538. <https://doi.org/10.1161/CIRCRESAHA.108.175976>.
45. Hoshina, K., Koyama, H., Miyata, T., Shigematsu, H., Takato, T., Dalman, R.L., and Nagawa, H. (2004). Aortic wall cell proliferation via basic fibroblast growth factor gene transfer limits progression of experimental abdominal aortic aneurysm. *J. Vasc. Surg.* 40, 512–518. <https://doi.org/10.1016/j.jvs.2004.06.018>.
 46. Kawai, N., Iwata, H., Shimabukuro, K., Ishida, N., Ogura, H., Umeda, E., and Doi, K. (2018). Suppression of aortic expansion and contractile recovery in a rat abdominal aortic aneurysm model by biodegradable gelatin hydrogel sheet incorporating basic fibroblast growth factor. *Heart Vessels* 33, 793–801. <https://doi.org/10.1007/s00380-017-1114-0>.
 47. Hu, Y., Chen, W., Li, C., Wang, X., Luo, J., and Cheng, B. (2022). LncRNA ANRIL facilitates vascular smooth muscle cell proliferation and suppresses apoptosis via modulation of miR-7/FGF2 pathway in intracranial aneurysms. *Neurocrit. Care* 36, 106–115. <https://doi.org/10.1007/s12028-021-01262-9>.
 48. Parma, L., Peters, H.A.B., Sluiter, T.J., Simons, K.H., Lazzari, P., de Vries, M.R., and Quax, P.H.A. (2020). bFGF blockade reduces intraplaque angiogenesis and macrophage infiltration in atherosclerotic vein graft lesions in ApoE3*Leiden mice. *Sci. Rep.* 10, 15968. <https://doi.org/10.1038/s41598-020-72992-7>.
 49. Liu, M.H., Tang, Z.H., Li, G.H., Qu, S.L., Zhang, Y., Ren, Z., Liu, L.S., and Jiang, Z.S. (2013). Janus-like role of fibroblast growth factor 2 in arteriosclerotic coronary artery disease: atherogenesis and angiogenesis. *Atherosclerosis* 229, 10–17. <https://doi.org/10.1016/j.atherosclerosis.2013.03.013>.
 50. Mao, Y., Liu, X.Q., Song, Y., Zhai, C.G., Xu, X.L., Zhang, L., and Zhang, Y. (2020). Fibroblast growth factor-2/platelet-derived growth factor enhances atherosclerotic plaque stability. *J. Cell. Mol. Med.* 24, 1128–1140. <https://doi.org/10.1111/jcmm.14850>.
 51. Dimcevski, G., Kotopoulos, S., Bjånes, T., Hoem, D., Schjøtt, J., Gjertsen, B.T., Biermann, M., Molven, A., Sorbye, H., McCormack, E., et al. (2016). A human clinical trial using ultrasound and microbubbles to enhance gemcitabine treatment of inoperable pancreatic cancer. *J. Control Release* 243, 172–181. <https://doi.org/10.1016/j.jconrel.2016.10.007>.
 52. Ramot, Y., Rotkopf, S., Gabai, R.M., Zorde Khvalevsky, E., Muravnik, S., Marzoli, G.A., Domb, A.J., Shemi, A., and Nyska, A. (2016). Preclinical safety evaluation in rats of a polymeric matrix containing an siRNA drug used as a local and prolonged delivery system for pancreatic cancer therapy. *Toxicol. Pathol.* 44, 856–865. <https://doi.org/10.1177/0192623316645860>.
 53. Zorde Khvalevsky, E., Gabai, R., Rachmut, I.H., Horwitz, E., Brunschwig, Z., Orbach, A., Shemi, A., Golan, T., Domb, A.J., Yavin, E., et al. (2013). Mutant KRAS is a drug-gable target for pancreatic cancer. *Proc. Natl. Acad. Sci. USA* 110, 20723–20728. <https://doi.org/10.1073/pnas.1314307110>.
 54. Huang, C.K., Kafert-Kasting, S., and Thum, T. (2020). Preclinical and clinical development of noncoding RNA therapeutics for cardiovascular disease. *Circ. Res.* 126, 663–678. <https://doi.org/10.1161/CIRCRESAHA.119.315856>.
 55. Abplanalp, W.T., Fischer, A., John, D., Zeiher, A.M., Gosgnach, W., Darville, H., Montgomery, R., Pestano, L., Allée, G., Paty, I., et al. (2020). Efficiency and target derepression of Anti-miR-92a: results of a first in human study. *Nucleic Acid Ther.* 30, 335–345. <https://doi.org/10.1089/nat.2020.0871>.
 56. Täubel, J., Hauke, W., Rump, S., Viereck, J., Batkai, S., Poetzsch, J., Rode, L., Weigt, H., Genschel, C., Lorch, U., et al. (2021). Novel antisense therapy targeting microRNA-132 in patients with heart failure: results of a first-in-human Phase 1b randomized, double-blind, placebo-controlled study. *Eur. Heart J.* 42, 178–188. <https://doi.org/10.1093/eurheartj/ehaa898>.
 57. Pelisek, J., Hegenloh, R., Bauer, S., Metschl, S., Pauli, J., Glukha, N., Busch, A., Reutersberg, B., Kallmayer, M., Trenner, M., et al. (2019). Biobanking: objectives, requirements, and future challenges-experiences from the Munich vascular Biobank. *J. Clin. Med.* 8, 251. <https://doi.org/10.3390/jcm8020251>.
 58. Stary, H.C., Chandler, A.B., Dinsmore, R.E., Fuster, V., Glagov, S., Insull, W., Jr., Rosenfeld, M.E., Schwartz, C.J., Wagner, W.D., and Wissler, R.W. (1995). A definition of advanced types of atherosclerotic lesions and a histological classification of atherosclerosis. A report from the Committee on Vascular Lesions of the Council on Arteriosclerosis, American Heart Association. *Arterioscler. Thromb. Vasc. Biol.* 15, 1512–1531. <https://doi.org/10.1161/01.atv.15.9.1512>.
 59. Redgrave, J.N., Gallagher, P., Lovett, J.K., and Rothwell, P.M. (2008). Critical cap thickness and rupture in symptomatic carotid plaques: the oxford plaque study. *Stroke* 39, 1722–1729. <https://doi.org/10.1161/STROKEAHA.107.507988>.
 60. Butler, A., Hoffman, P., Smibert, P., Papalexi, E., and Satija, R. (2018). Integrating single-cell transcriptomic data across different conditions, technologies, and species. *Nat. Biotechnol.* 36, 411–420. <https://doi.org/10.1038/nbt.4096>.
 61. Stuart, T., Butler, A., Hoffman, P., Hafemeister, C., Papalexi, E., Mauck, W.M., 3rd, Hao, Y., Stoeckius, M., Smibert, P., and Satija, R. (2019). Comprehensive integration of single-cell data. *Cell* 177, 1888–1902.e21. <https://doi.org/10.1016/j.cell.2019.05.031>.
 62. Barron, M., and Li, J. (2016). Identifying and removing the cell-cycle effect from single-cell RNA-Sequencing data. *Sci. Rep.* 6, 33892. <https://doi.org/10.1038/srep33892>.
 63. Hafemeister, C., and Satija, R. (2019). Normalization and variance stabilization of single-cell RNA-seq data using regularized negative binomial regression. *Genome Biol.* 20, 296. <https://doi.org/10.1186/s13059-019-1874-1>.
 64. Perez-Riverol, Y., Bai, J., Bandla, C., García-Seisdedos, D., Hewapathirana, S., Kamatchinathan, S., Kundu, D.J., Prakash, A., Frericks-Zipper, A., Eisenacher, M., et al. (2022). The PRIDE database resources in 2022: a hub for mass spectrometry-based proteomics evidences. *Nucleic Acids Res.* 50, D543–D552. <https://doi.org/10.1093/nar/gkab1038>.

Supplemental Information

Targeting long non-coding RNA *NUDT6* enhances smooth muscle cell survival and limits vascular disease progression

Hanna Winter, Greg Winski, Albert Busch, Ekaterina Chernogubova, Francesca Fasolo, Zhiyuan Wu, Alexandra Bäcklund, Bohdan B. Khomtchouk, Derek J. Van Booven, Nadja Sachs, Hans-Henning Eckstein, Ilka Wittig, Reinier A. Boon, Hong Jin, and Lars Maegdefessel

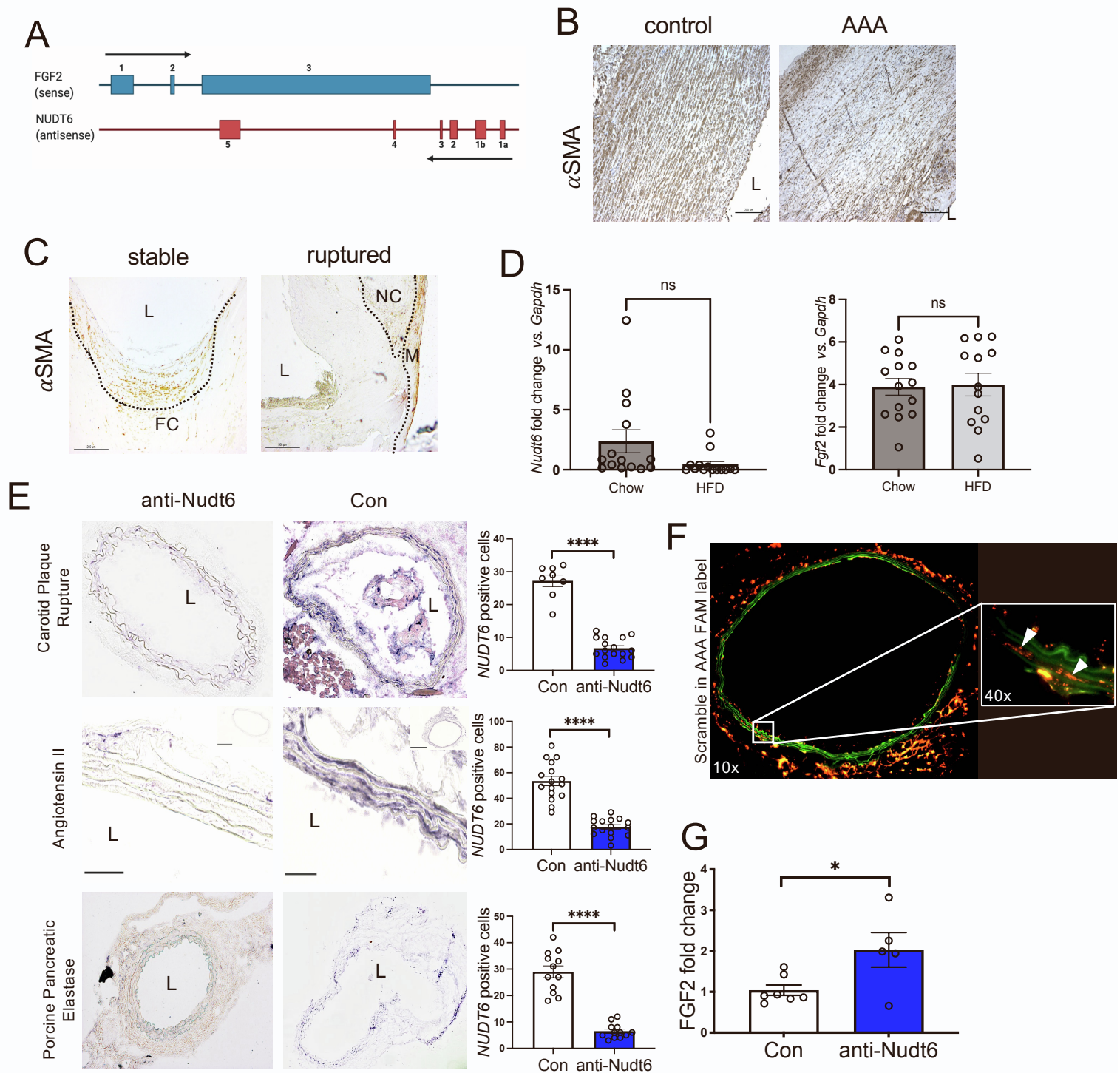


Figure S1

(A) Scheme adapted from ²⁴ showing the common overlap of *NUDT6* and *FGF2* transcripts and respective exons. (B-C) Immunohistochemical staining for α SMA of stable and ruptured carotid lesions (B) and control aorta and AAA (C) show a similar expression pattern compared to *FGF2*. (D) qRT-PCR analysis of aortic arches from *ApoE*^{-/-} mice fed either chow diet or high fat diet (HFD) for 12 weeks show no significant change in *Nudt6* and *Fgf2* expression. (E) Confirmatory *In situ* hybridization of *Nudt6* in the three mouse models with signal quantification for *Nudt6* signal (4 high power fields per image, N=8-16 counts in total). (F) Fluorescent FAM-labelled scramble particles show successful transmission of locked nucleic acid – oligos to the intima media of the abdominal aorta via Ultrasound targeted microbubble destruction (UTMD). (G) qRT-PCR analysis of abdominal aorta show increased *Fgf2* levels in anti-*Nudt6* treated AngII mice (n=5 per group). Quantitative data are shown as mean + SEM. **p*<0.05; *****p*<0.0001. Significance is determined using one-tailed Student's t-test.

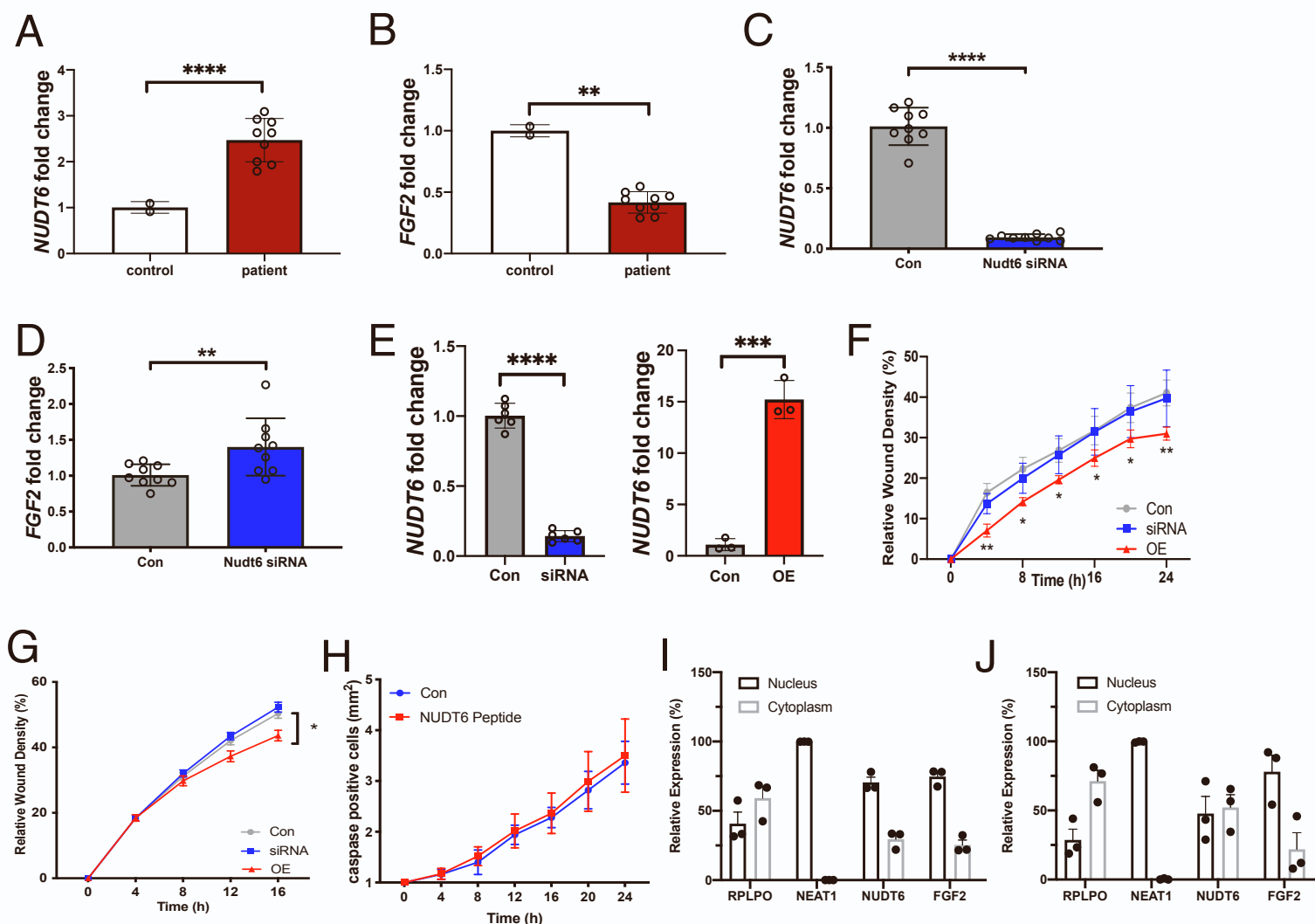


Figure S2

(A-B) *NUDT6* (A) and *FGF2* (B) mRNA expression after qRT-PCR in 3 different patient-derived aortic VSMCs (n=3 per patient). (C-D) Knocking down *NUDT6* via siRNA in patient-derived aortic VSMCs led to a downregulation of *NUDT6* (C) mRNA but had a rescuing effect on *FGF2* (D) mRNA levels (n=3 per patient). (E) Confirmatory qRT-PCR for *NUDT6* after *NUDT6* knockdown and overexpression shows significant deregulation in hAoSMCs (n=6 per group). (F-G) Live cell imaging of both hCtSMCs (F) and hAoSMCs (G) show impaired migratory capacity of cells receiving overexpression vector for *NUDT6*. *NUDT6*-siRNA-treated cells behave as scramble control (n=3 per group). (H) Dynamic live-cell imaging of hCtSMCs treated with *NUDT6* peptide does not have an effect on apoptosis (n=5 per group). (I-J) Nucleocytoplasmic fractionation of hCtSMCs (I) and hAoSMCs (J) show intracellular distribution of *NUDT6* and *FGF2* compared to nuclear-expressed *NEAT1* and cytoplasmic expressed *RPLPO* (n=3 per group). Quantitative results are shown as mean+SEM. *p<0.05; **p<0.01; ****p<0.0001. Significance was calculated using One-tailed Student's t-test (A-E, I-J) or two-way ANOVA with Tukey (F-H).

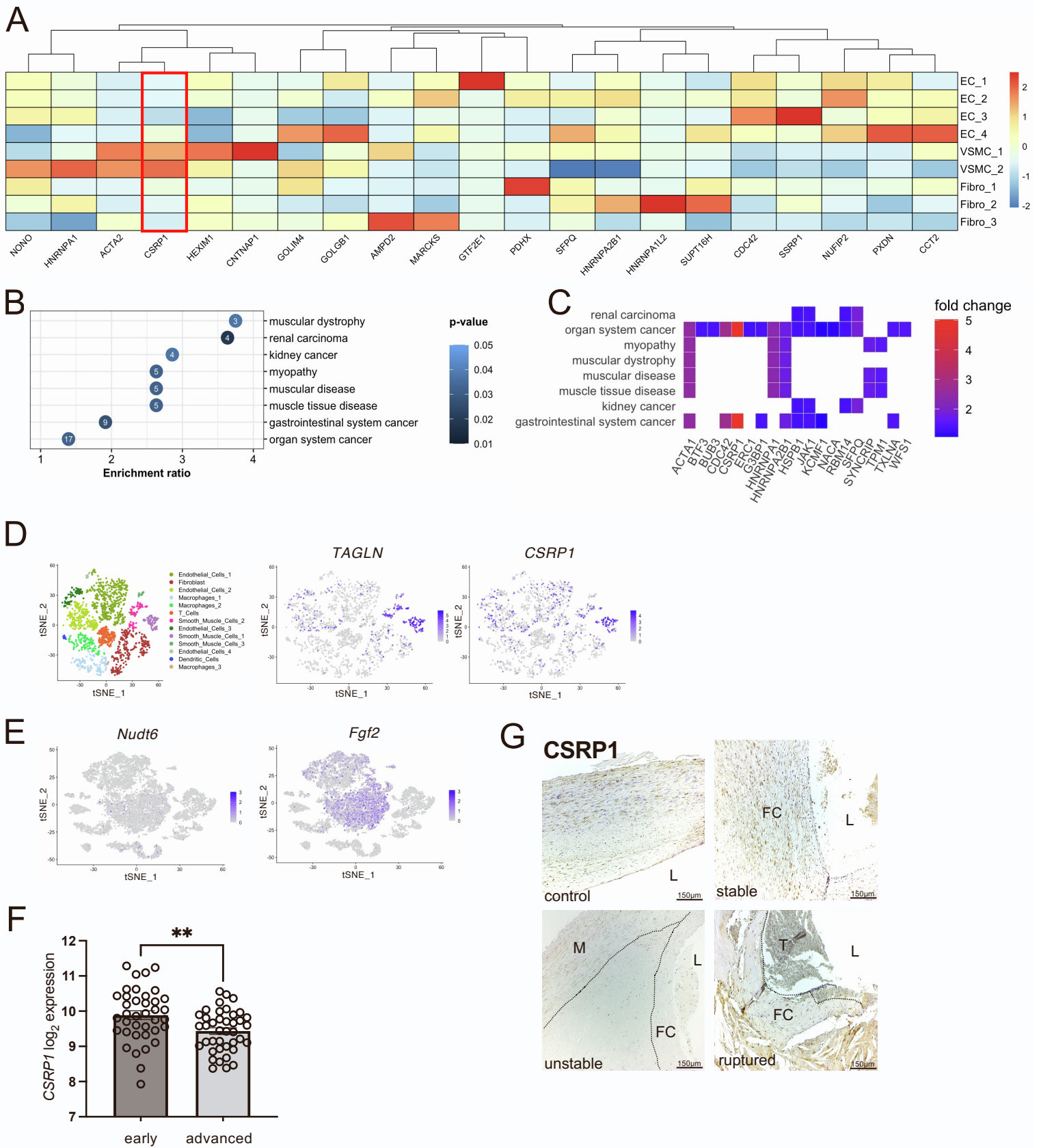


Figure S3

(A) Heat map showing the abundance and expression of CSRP1 in VSMCs and ECs from human single-cell RNA sequencing experiments (Figure 5B). (B) Significant enrichment of potential NUDT6:protein interaction partners (Figure 5A) within several Disease Ontology datasets. (C) Regulation of potential NUDT6:protein interaction partners within specific Disease Ontology datasets shown in (B). (D) tSNE plots of scRNA Sequencing data from porcine AAA with expression plots of Transgelin (TAGLN) and CSRP1. AAAs were induced via PPE. (E) t-SNE plots of scRNA Sequencing data from murine AAA with expression plots of *Nudt6* and *Fgf2*. (F) *CSRP1* expression in early and advanced carotid lesions of a bulk sequencing dataset generated in our lab. (G) *CSRP1* protein expression in control carotid, stable, unstable and ruptured carotid lesions (L=lumen, M=Media, T=Thrombus, FC=Fibrous Cap). Quantitative data are shown as mean + SEM. ** $p < 0.01$; Significance is determined using two-tailed paired Student's t-test.

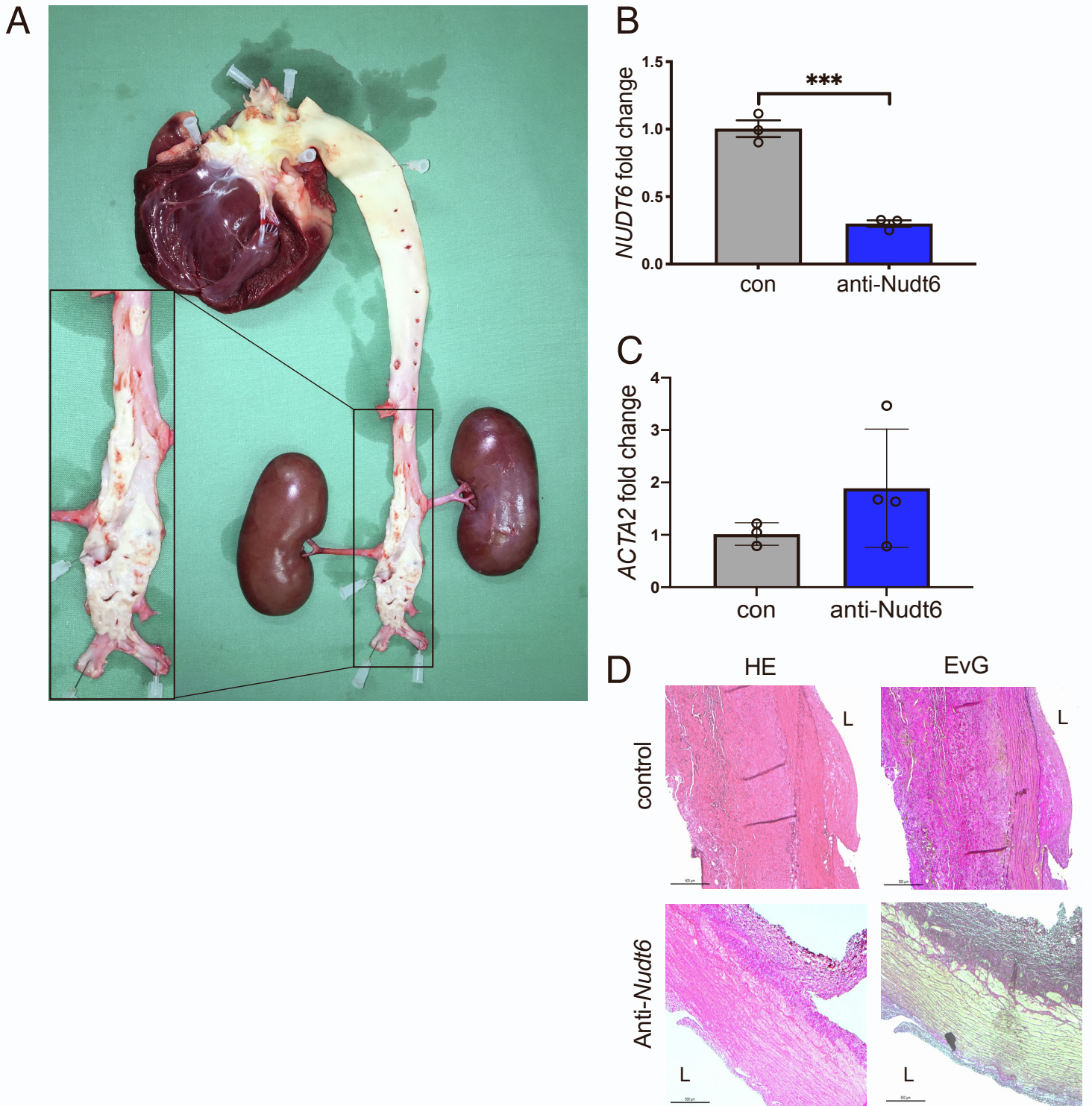


Figure S4

(A) Representative image of the heart, aorta, and kidneys of an LDLR^{-/-} pig with an enlarged image of the abdominal aorta. **(B)** Porcine aortic fibroblasts (n=3) treated with designed porcine *in vivo* locked nucleic acid against *NUDT6* show downregulation of *NUDT6* after treatment. © qRT-PCR of whole porcine aortic tissue (n=3-4) shows an increase in *ACTA2* mRNA. **(D)** HE and EvG stainings of the abdominal aorta anti-*NUDT6* treated (n=4) and control (n=3) animals. Quantitative data are shown as mean + SEM. ***p<0.001. Significance is determined using one-tailed Student's t-test **(B-C)**.

Table S1Table of the top 20 identified *NUDT6*-RNA Pulldown Targets.

	Protein names	Gene names	Fold enriched <i>NUDT6</i> vs CTRL
1	Cysteine and glycine-rich protein 1	CSRP1	32.588
2	General transcription factor IIE subunit 1	GTF2E1	11.126
3	Cell division control protein 42 homolog	CDC42	6.958
4	FACT complex subunit SPT16	SUPT16H	5.890
5	Nuclear fragile X mental retardation-interacting protein 2	NUFIP2	5.821
6	Actin, alpha skeletal muscle;Actin, alpha cardiac muscle 1;Actin, gamma-enteric smooth muscle;Actin, aortic smooth muscle	ACTA1;ACTC1;ACTG2; ACTA2	5.646
7	Peroxidasin homolog	PXDN	5.446
8	FACT complex subunit SSRP1	SSRP1	5.404
9	Heterogeneous nuclear ribonucleoprotein A1;	HNRNPA1;HNRNPA1L2	4.940
10	T-complex protein 1 subunit beta	CCT2	4.879
11	Protein HEXIM1	HEXIM1	4.792
12	Non-POU domain-containing octamer-binding protein	NONO	4.729
13	Myristoylated alanine-rich C-kinase substrate	MARCKS	3.975
14	Golgi integral membrane protein 4	GOLIM4	3.930
15	Contactin-associated protein 1	CNTNAP1	3.741
16	AMP deaminase 2	AMPD2	3.662
17	Splicing factor, proline- and glutamine-rich	SFPQ	3.641
18	Heterogeneous nuclear ribonucleoproteins A2/B1	HNRNPA2B1;HNRPA2B1	3.421
19	Golgin subfamily B member 1	GOLGB1	3.384
20	Pyruvate dehydrogenase protein X component, mitochondrial	PDHX	3.331